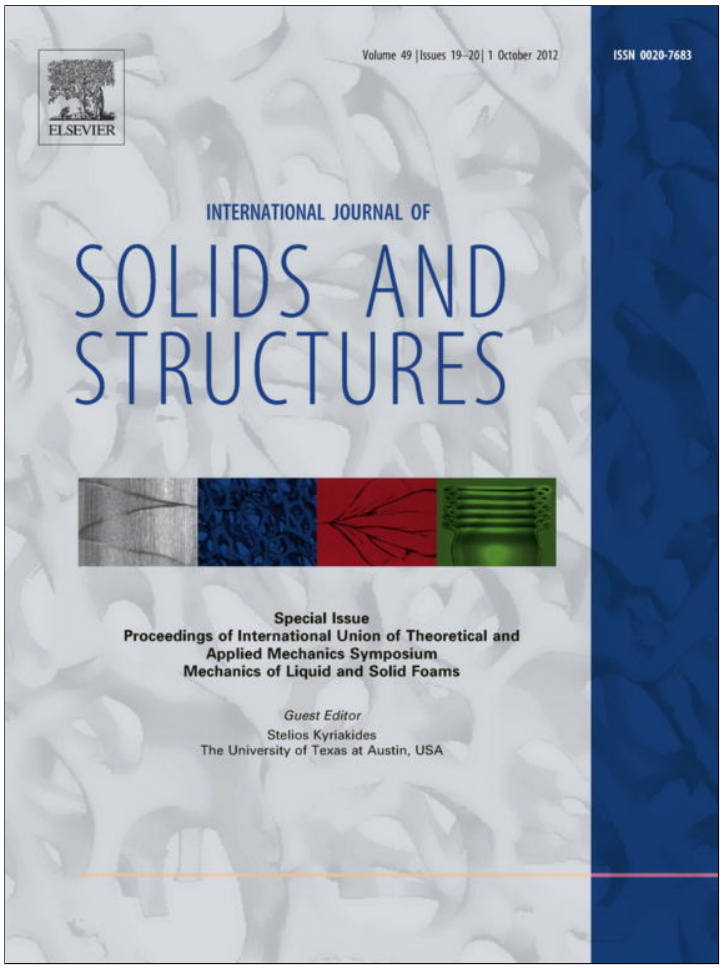

International Journal of Solids and Structures 49 (2012) 2714–2732

Contents lists available at SciVerse ScienceDirect

International Journal of Solids and Structures

journal homepage: www.elsevier.com/locate/ijsolstr

Impact of material processing and deformation on cell morphology and mechanical behavior of polyurethane and nickel foams

A. Burteau [a], F. N'Guyen [a], J.D. Bartout [a], S. Forest [a,*], Y. Bienvenu [a], S. Saberi [b], D. Naumann [b]

[a] MINES ParisTech, Centre des matériaux, CNRS UMR 7633, BP 87, 91003 Evry Cedex, France
[b] Inco Special Products, 2101 Hadwen Road, Mississauga, ON, Canada L5K 2L3

ARTICLE INFO

Article history:
Available online 15 June 2012

Keywords:
Metal foam
Nickel foam
PU foam
Polyurethane foam
Cell morphology
Cell deformation
Micro-tomography
Material processing
Finite element
Plasticity
Hyperelasticity
Diesel particulate filtering
Architectured material

ABSTRACT

The cell morphology and mechanical behavior of open-cell polyurethane and nickel foams are investigated by means of combined 3D X-ray micro-tomography and large scale finite element simulations. Our quantitative 3D image analysis and finite element simulations demonstrate that the strongly anisotropic tensile behavior of nickel foams is due to the cell anisotropy induced by the deformation of PU precursor during the electroplating and heat treatment stages of nickel foam processing. *In situ* tensile tests on PU foams reveal that the initial main elongation axis of the cells evolves from the foam sheet normal direction to the rolling direction of the coils. Finite element simulations of the hyperelastic behavior of PU foams based on real cell morphology confirm the observation that cell struts do not experience significant elongation after 0.15 tensile straining, thus pointing out alternative deformation mechanisms like complex strut junctions deformation. The plastic behavior and the anisotropy of nickel foams are then satisfactorily retrieved from finite element simulations on a volume element containing eight cells with a detailed mesh of all the hollow struts and junctions. The experimental and computational strategy is considered as a first step toward optimization of process parameters to tailor anisotropy of cell shape and mechanical behavior for applications in batteries or Diesel particulate filtering.

1. Introduction

Open cell nickel foams belong to the most widely spread cellular metals because of their use in NiMH battery applications (Ashby et al., 2000). The material processing of nickel foams is constantly optimized in order to reduce the cost of mass production of mm-thick sheets. The processing begins with the electroplating of a polyurethane (PU) foam precursor, possibly preceded by a Ni magnetron sputtering stage to make the PU foam sufficiently conductive for the electroplating. At the end of the electroplating the metallic foam is rather brittle and a two stage heat treatment is necessary to restore material ductility. During the first stage under air and limited to 600 °C at most, the polyurethane material is burnt which gives this nickel foam product its special microstructure made of hollow struts. During the second stage at higher temperature (around 1000 °C) and under a reducing atmosphere (N2–H2), the oxide films are reduced and the grain structure is controlled. The mechanical properties of nickel foams are of the utmost importance since the struts should not be damaged during the compaction of the electrode powder and the final coiling in the battery container.

Nickel foams display a strongly anisotropic mechanical behavior regarding both the stress level and the final ductility, as evidenced by Badiche et al. (2000). The objective of the present work is to quantitatively identify the reasons for such an anisotropic behavior from the knowledge of the cell morphology and mechanical behavior of PU foam precursor and of the material processing route and nickel mechanical behavior. The anisotropic response will be shown to arise from an interplay between the straining of the PU foam during electroplating and the quasi-linear hardening of the nickel walls of the struts. Such a study represents a first necessary step towards tailoring the elastic–plastic properties of nickel foam products for battery or more advanced applications like Diesel particulate filtering (DPF).

For that purpose, we will resort to systematic quantitative analysis of X-ray micro-tomography images. X-ray micro-tomography came out in the past decade as an efficient tool for the detailed characterization of the morphology of foams (Buffière et al., 1999; Maire et al., 2001; Vicente et al., 2006). Micro-tomography is advantageously combined with *in situ* mechanical testing as described by Buffière et al. (2010). Dillard et al. (2005) determined the volume, size and orientation of about 150 cells in a nickel open-cell foam. Jang et al. (2008) completed the description of polyurethane and

* Corresponding author. Tel.: +33 1 60 76 30 51; fax: +33 1 60 76 31 50.
E-mail addresses: samuel.forest@ensmp.fr, samuel.forest@mat.ensmp.fr (S. Forest).

0020-7683/$ - see front matter © 2012 Elsevier Ltd. All rights reserved.
http://dx.doi.org/10.1016/j.ijsolstr.2012.05.026

aluminium foams by adding the measured variation of ligament cross-sectional area along the ligament length. The population of studied cells is usually limited to one or two hundreds like in Montminy et al. (2004). More systematic analysis accounting for thousands of cells will be provided in the present work, thus complementing the extensive micro-tomography data by Vicente et al. (2006) for nickel foams.

The nature and processing of the polyurethane (PU) foam has a significant impact on the final properties of the nickel foam. That is why the PU also is the subject of the present study. Micro-tomography has been recently applied by Ridha and Shim (2008) to the microstructure and tensile properties of anisotropic rigid polyurethane foams which display elongated cells in the rise direction, referring to the PU foaming process and to the peeling of the blocks, as depicted in the PU material of the present study. However, no quantitative analysis of the 3D data was attempted in the latter reference but individual strut bending mechanism was noticed during *in situ* testing. An original contribution of the present work is to compare the cell morphology of various PU foam precursors, in terms of pore size, to that of the final nickel foam product. The evidenced differences will give valuable indications on the subsequent mechanical behavior. The different pore sizes (350, 450, 580 and 1200 μm) and corresponding foam relative densities are considered in order to provide sufficient statistical representativity of the results and evidence possible pore size effects.

Most studies on metal and polymer cellular materials deal with their compression behavior due to applications related to crash absorption and cushioning (Youssef et al., 2005; Gong et al., 2005). The analysis by Diologent et al. (2009) of open-cell aluminium–nickel foams also deals with the compression behavior. In contrast, a recent experimental analysis of the tensile behavior of open-cell nickel foams has been provided by Aly (2010). The PU and nickel foams considered in the present work are produced in the form of thin sheets so that they are mainly subjected to in-plane tensile loading during the process and for the mentioned applications. Compression within the thickness of this product has also been investigated but the results are not reported in the present work. Several papers provide experimental and modeling results on the behavior of open-cell foams under compression, as done by Gong et al. (2005). But none of these studies provide quantitative estimation of the variation of geometric characteristics with deformation. Over the course of this research, we followed quantitatively the evolution of the volume, size and orientation of the cells as well as the evolution of the estimated strut length during tensile tests.

The micro-tomography analysis is combined with large scale finite element simulations based on the real foam morphology following a computational strategy initiated by Cailletaud et al. (2003) for general heterogeneous materials and by Youssef et al. (2005) for foams. When the porous material possesses a periodic microstructure like in architectured materials made of hollow spheres or cylinders, a finite element model can be easily built in 3D and applied to predict the non-linear mechanical behavior as done for instance by Marcadon and Feyel (2009) including experimental validation of the macroscopic response. It assumes that the local mechanical behavior of the dense material constituent is sufficiently known, which is not always the case both for metal and polymer foams. This computational strategy has first been developed successfully for metal closed cell foams in Youssef et al. (2005) and Gagliardi et al. (2009) and syntactic foams in Adrien et al. (2007). We will apply it systematically for both open-cell PU and nickel foams, providing new results on these wide-spread materials.

Cellular solids are highly contrasted heterogeneous materials for which the question of the representative volume element size for determining morphological and mechanical properties strongly depends of the detailed microstructure and local constitutive behavior. Representative volume element size for cellular materials was previously studied mainly for model random microstructures like beam networks and remains largely unspecified for real morphologies, except by Youssef et al. (2005) where this question was addressed. The present work will bring some new insight in this topic both for finite strain elasticity and plasticity.

The mechanical behavior of PU foams has been mainly studied from the macroscopic perspective by developing suitable hyperelastic constitutive equations for the effective response of the material (Attard and Hunt, 2004). A hyperelastic macroscopic model was recently formulated by Dai et al. (2011) based on a unit cell model made of four-bar tetrahedral structure, also accounting for compression buckling. The combined micro-tomography and finite element analysis has been recently applied to rather brittle syntactic foams by Adrien et al. (2007). In the present work, the micromechanical analysis is performed from the real morphology and dense PU constitutive behavior to predict the overall response and compare with experimental results. However the analysis remains confined to intermediate strain ranges which are relevant for the final behavior of nickel foams, which is the main objective of the work. The computational tool used in this work for finite strain behavior of polymers is taken from original works by Laiarinandrasana et al. (2003) and Cantournet et al. (2009).

The outline of the paper is as follows. The material description, *in situ* testing method and the 3D image analysis tools are reported in Section 2. A detailed quantitative analysis of the initial precursor PU foam morphology and that of the produced nickel foam are provided in Section 3. The evolution of cell shape and orientation during tensile deformation is investigated for PU and nickel foams. The change in strut length during deformation is also quantified by a thorough analysis of the skeleton of the initial and deformed foams. The results are provided from a statistical point of view. However the response of some individual cells is also followed in order to determine some local deformation mechanisms. Section 4 is dedicated to the finite element analysis of the hyperelastic response of a cluster of PU cells. The predicted overall response and the evolution of local characteristics like strut length are compared to experimental results giving insight in the intimate foam deformation modes. We also define quantitatively in Section 4.2 the concept of cell micro-deformation which we can compare to the overall applied deformation. The same computational strategy is applied to the case of the elastic–plastic behavior of nickel foams in Section 5. We take advantage of a precise knowledge of the constitutive behavior of the polycrystalline nickel material building up the strut walls, earned in a previous work (Goussery et al., 2004). The presented intensive non-linear finite element simulations are finally used to predict the anisotropic response of the nickel foam.

2. Experimentals

The deformation of foams with different base materials (polyurethane and nickel) and various average pore sizes, all provided by INCO SP, were studied. Tensile tests coupled with X-ray micro-tomography were performed to determine and compare the morphological characteristics in the different material processing stages of the samples. This section presents the materials, the experimental set-up and the procedures used.

2.1. Material description

The nickel foam processing route can be divided into five main steps. Firstly, a polyurethane foam plate with the desired thickness and porosity for the final product is selected as a foam template. The polyurethane foams are produced in huge blocks ($1 \times 1 \times 60$ m) which are pealed perpendicular to the cell *rise* direction,

along the sheet thickness. These sheets, whose thickness can be chosen between 1 and 3 mm, become the precursors for the nickel foams. Cathodic magnetron nickel sputtering is then used to cover the foam template with a thin layer of nickel. This 0.1 μm thick nickel deposit is sufficient to make the foam electrically conductive. An electroplating technique is then used for the deposition of a 10 μm thick nickel layer. Nickel is electroplated on the PU foams; a heat treatment is applied to this composite material for recrystallization of the deposit and burning of the PU *skeleton*. The polymer template is burnt and a final heat treatment is carried out to improve the ductility of the foam. This is the reason why the nickel struts are hollow in the final product although the struts of the PU cells are full. Finally, nickel foams are packaged and sold in the form of coils.

Fig. 1 shows the final product, a nickel open-cell foam with hollow struts (see Walther et al., 2008 for more details on material processing).

The available PU foams for this study have expected mean pore sizes of 350, 580 and 1200 μm (referred to as PU350, PU580 and PU1200). The corresponding thicknesses of the sheets respectively are 1.3, 1.9 and 3.0 mm. Their relative densities respectively are 4.5%, 2.9% and 2.7%, as indicated in Table 1. The morphological analysis is focused on the Ni580 nickel foam which has an expected pore size of 580 μm, a sheet thickness of 1.9 mm, like the PU580 precursor, and a relative density of 3.4%. The wall thickness of the hollow struts in the Ni580 is about 5–10 μm depending on the area and the quantity of nickel deposited there. Large pores are easier to image in 3D but the statistics is not sufficient due to the number of cells within the thickness limited to 1–3. That is why different pore sizes are considered in the analysis to have different insights on the morphology.

As these foams are manufactured in the form of coils, we define the associated reference frame (RD,TD,ND), where RD is the *rolling* (or *coiling*) direction, TD is the *transverse* direction and ND is the *normal* (or *rise*) direction (see Fig. 2). The initial huge block are cut into sheets perpendicular of the rise direction of the PU foam, i.e. the ND direction. This explains why the cells will be shown to be initially elongated in the ND direction. The initial PU foam morphology is transverse isotropic so that the distinction between RD and TD is a consequence of the nickel foam processing.

The nickel foams display a strongly anisotropic mechanical behavior, as shown by the tensile curves of Fig. 3 for Ni580. The tensile curves are characterized by non-linear hardening just after yielding followed by linear hardening until fracture. The stress levels reached in tension along RD are almost twice higher than for tension in direction TD. In contrast, ductility is almost twice higher for TD than RD. A similar behavior was reported by Aly (2010).

Table 1
General characteristics of the studied foams.

Foam name	Expected pore size (μm – ppi)	Relative density ρ/ρ_s (%)
PU350	350 – 73	4.5 ± 0.1
PU580	580 – 44	2.9 ± 0.1
PU1200	1200 – 22	2.7 ± 0.1
Ni450	450 – 56	3.2 ± 0.1
Ni580	580 – 44	3.4 ± 0.1

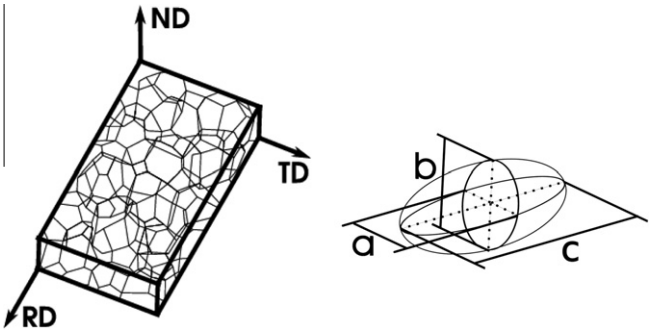

Fig. 2. Foam reference frame (left); equivalent ellipsoid for each cell and its parameters *a*, *b* and *c* (right).

2.2. In situ mechanical testing

The X-ray micro-tomography platform of the ID19 beam line at the European Synchrotron Radiation Facility in Grenoble gives the possibility of using additional apparatus to perform various types of tests. A homemade tensile cylinder (see Fig. 4 (left)) has been used to perform *in situ* tensile tests with PU and Ni foams. Its central PMMA tube is transparent to X-ray; the lower grip is fixed whereas the upper grip can be moved axially. Basically, a scan is made of 900 radiographs over a 180° rotation using a peak energy of 15/30 keV for PU/Ni specimens, respectively. It lasts about 15 min thanks to an exposure time of about 1 s. The specimen size was 6–7 mm in width and 100–120 mm in height. The scanned zone was $8 \times 8 \times 8\ mm^3$ for 1624×1624 pixels resulting in a 5 μm pitch resolution. The reconstructed images were 4.1 Gb large.

Fig. 4 (right) depicts the experimental testing procedure. A scan of the sample in the initial state is first acquired. After that, the upper grip is displaced to obtain a chosen macroscopic deformation ε: 15% for the PU specimens and 3% for the Ni specimens. Next, the set-up position is adjusted by moving downward the rotating

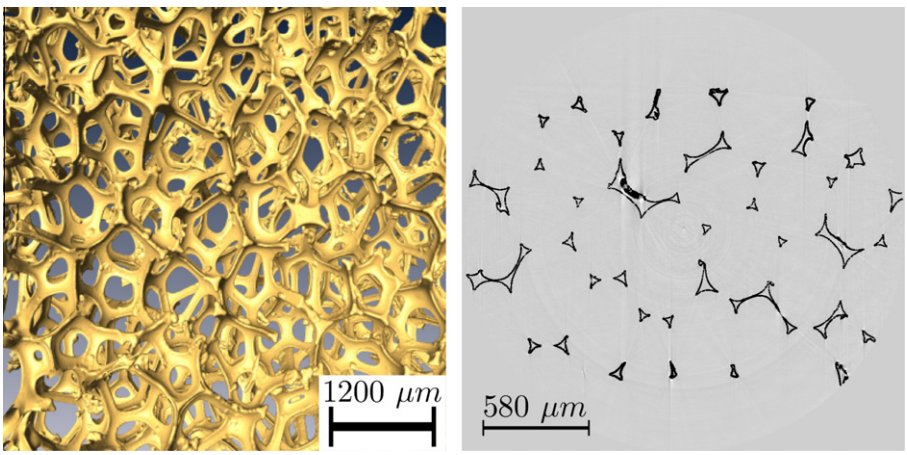

Fig. 1. Tomography data: 3D surface rendering (left) of a Ni1200 sample and a typical grey level 2D slice (right) taken out of the 2D image stack of a Ni580 sample.

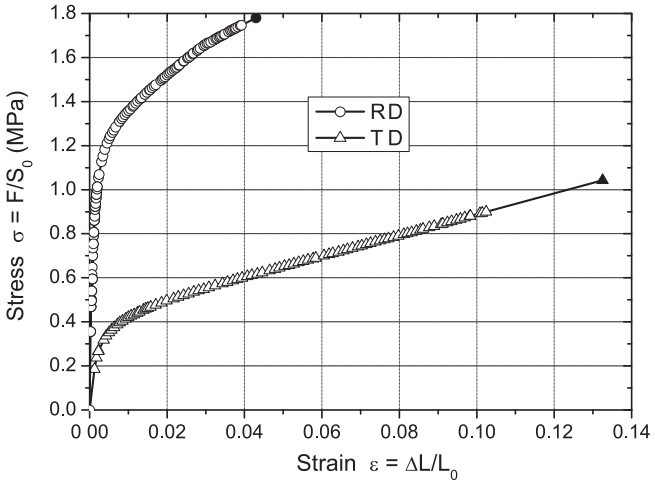

Fig. 3. Tensile behavior of the Ni580 in the RD and TD direction.

support of about $u = \varepsilon h$, where h is an estimation of the mean height of the initially scanned region. Finally, a scan of the sample in the deformed state is acquired. By following this procedure, we succeeded in scanning the same pores in their initial and deformed states and thus it gave us the possibility of characterizing the deformation mechanism of the foams.

All the *in situ* tensile tests were performed in the direction RD for PU and nickel foams.

2.3. 3D image analysis

We used essentially the same 3D image analysis techniques as Dillard et al. (2005) and Vicente et al. (2006). The starting tomography data is a 3D grey tone volume. As the linear attenuation coefficient of air, nickel and polyurethane are significantly different, the grey-level distribution of the images is bimodal. A simple threshold on the histograms is used to generate binary images. Before building the segmentation of the cells, the hollow struts of the nickel foams are to be filled in by straightforward morphological operations made on the 2D images. The 3D segmentation procedure is divided into three main steps. First, the distance map is computed according to Serra (1988). Secondly, the markers, one per cell, are determined in one step following Lantuéjoul and Maisonneuve (1984). Note that in Vicente et al. (2006), the authors used topological conditions to eliminate *bad* markers afterwards. Once the watershed has been constructed from these markers, the open cells are closed and isolated in 3D (Meyer and Beucher, 1990). The inertia tensors of these isolated pores are then computed. The resulting eigen-vectors and main axes provide a representation of the cell by equivalent ellipsoids. The main axes are defined in Fig. 2 (right) with $a \leqslant b \leqslant c$ thus ordered. This method, developed by Dillard et al. (2005), allowed us to follow in particular the evolution of the volume, size and orientation of the cells during deformation.

One of the largest population of cells studied is presented in Vicente et al. (2006) but (Dillard et al., 2005) remains (to our knowledge) one of the few studies of the evolution of foam morphology during tension. Whereas 150 nickel foam cells were analyzed by Dillard et al. (2005), the statistical analysis is here extended to about 1700 cells for the PU350, 900 cells for the PU580, 150 cells for the PU1200 and 620 cells for the Ni580, as indicated in Table 2, thus delivering unprecedented statistical database for PU and metal foams.

We also determine the skeleton of 3D foam images with filled struts, following a procedure explained in Dillard et al. (2005). From the skeleton, we identify the nodes of each cell, defined as the junctions between struts. From the nodes and the known connections a beam network is built from which each strut length is determined.

3. Evolution of cell morphology during processing and deformation

The geometrical characteristics of a foam are essential for quantitatively accurate predictions of all physical properties as shown by Gong et al. (2005) and Jang et al. (2008). Cell shape and size are characterized in this work by the inertia tensor of each individual cell. They have been determined at different strain levels by means of *in situ* X-ray micro-tomography, thus providing information about the evolution of cell shape during material processing including electroplating and heat treatment for which it is expected that deformation occurs due to the applied coiling force.

3.1. Initial foam morphology

This study deals with a set of PU and Ni foams covering a range of cell sizes from 350 to 1200 μm (see Table 1 for conversion in ppi) and with relative densities in the range of 2.7–4.5%. Table 2 summarizes the values of all the parameters determined for PU580 and Ni580, PU350 and PU1200 in their initial and deformed states. Fig. 5 displays the length distributions of the axes a, b and c of the equivalent ellipsoids for PU580 and Ni580. Fig. 6 shows the cell volume distribution in PU580 and Ni580. The corresponding curves for PU350 and PU1200 are similar to the previous ones and therefore are not shown here. First, we describe the initial morphology of

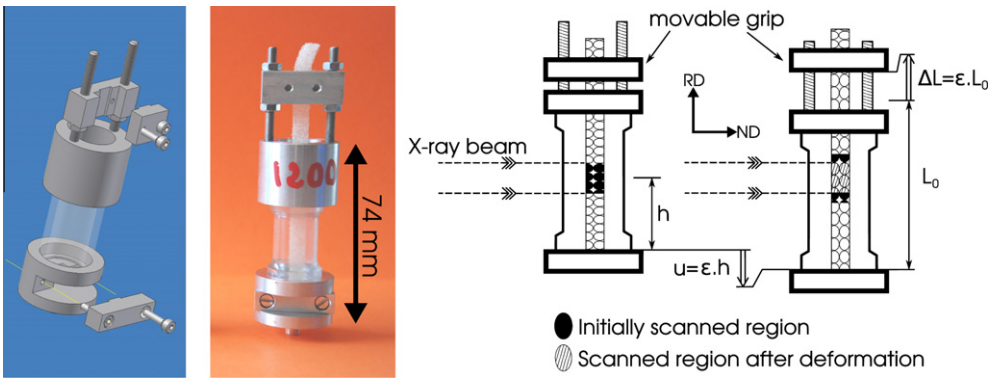

Fig. 4. Drawing of the specific device for *in situ* tensile tests (left); setup for a scan of a PU foam sample in the deformed position (middle). Procedure of the *in situ* tensile tests (right): first, scan of the sample in the initial state; next, deformation of the sample; then, translation of the set-up position; finally, scan of the deformed sample.

Table 2
Overall morphology of the cells in PU580, Ni580, PU350, PU1200 and their deformed states. The numbers of analyzed cells and struts are also indicated for each material.

Unit	a μm	b μm	c μm	c/a –	V_{mean} mm^3	$2R_{eq}$ μm	L_{strut} μm
PU580 – 954 cells – 14501 struts							
Mean value	431 ± 5	496 ± 5	611 ± 5	1.42	0.065	498 ± 5	186 ± 5
Standard deviation	93	92	136	–	0.034	–	173
PU580 + 15% – 872 cells – 13021 struts							
Mean value	395 ± 5	503 ± 5	629 ± 5	1.59	0.062	490 ± 5	188 ± 5
Standard deviation	90	105	138	–	0.035	–	181
Ni580 – 625 cells – 9640 struts							
Mean value	446 ± 5	548 ± 5	649 ± 5	1.46	0.078	530 ± 5	205 ± 5
Standard deviation	90	105	128	–	0.040	–	193
Ni580 + 3% – 613 cells – 9581 struts							
Mean value	440 ± 5	552 ± 5	650 ± 5	1.48	0.078	530 ± 5	207 ± 5
Standard deviation	89	111	129	–	0.041	–	197
PU350 – 1742 cells – 25539 struts							
Mean value	293 ± 5	336 ± 5	444 ± 5	1.52	0.021	344 ± 5	128 ± 5
Standard deviation	87	87	132	–	0.017	–	76
PU350 + 15% – 1607 cells – 23178 struts							
Mean value	285 ± 5	362 ± 5	429 ± 5	1.51	0.021	344 ± 5	132 ± 5
Standard deviation	89	105	111	–	0.018	–	81
PU1200 – 167 cells – 3215 struts							
Mean value	870 ± 5	990 ± 5	1283 ± 5	1.47	0.557	1021 ± 5	399 ± 5
Standard deviation	145	116	542	–	0.243	–	448
PU1200 + 15% – 147 cells – 2820 struts							
Mean value	820 ± 5	1068 ± 5	1282 ± 5	1.56	0.559	1022 ± 5	383 ± 5
Standard deviation	159	193	221	–	0.205	–	468

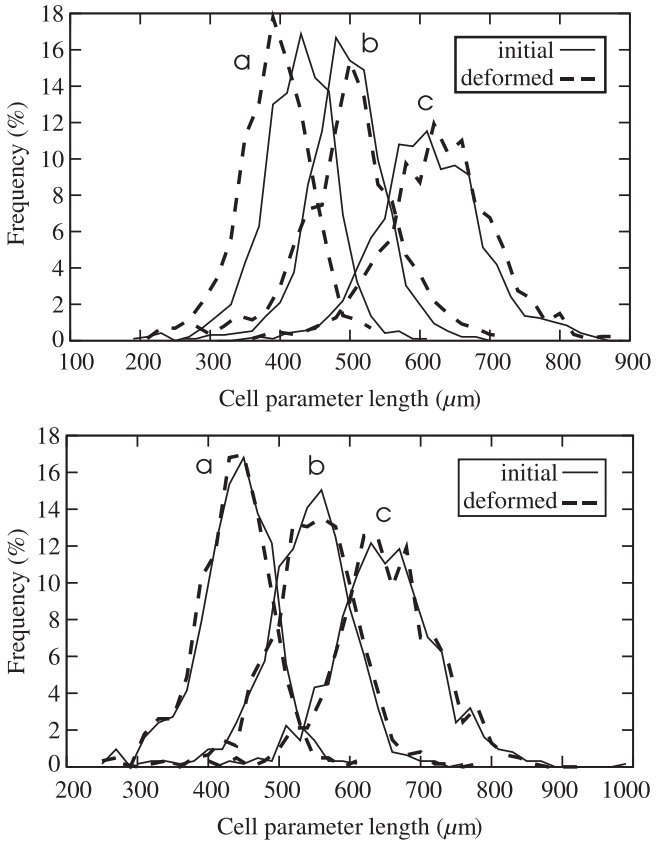

Fig. 5. Length distribution of the main axes of the equivalent ellipsoid for cells in a PU580 sample (top) and a Ni580 sample (bottom) in their initial and deformed states.

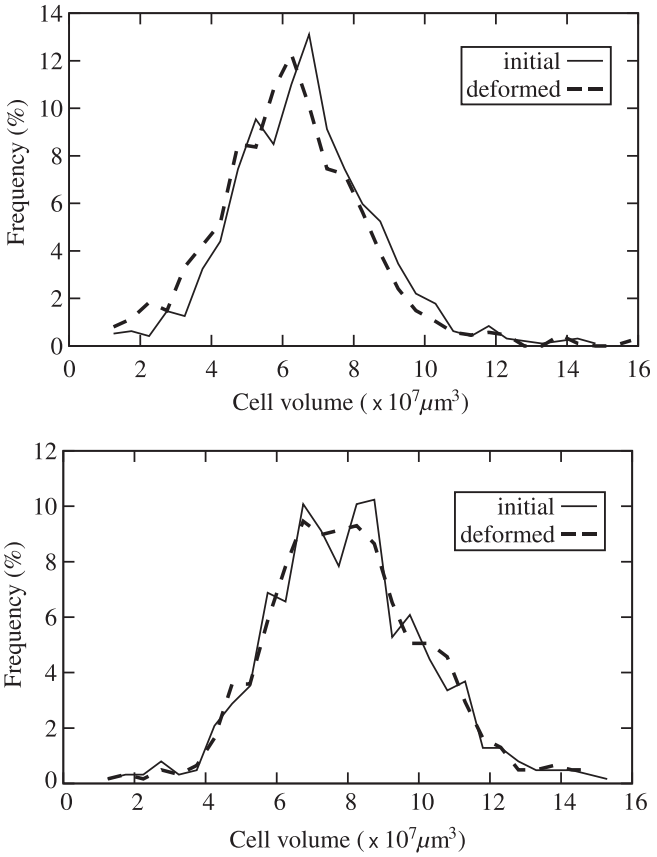

Fig. 6. Volume distribution of the cells in a PU580 sample (top) and a Ni580 sample (bottom) in their initial and deformed states.

the precursors PU350, PU580 and PU1200 precursors and we then compare it to the morphology of the final product Ni580.

The mean cell volume is determined as the number of voxels contained in the isolated pack multiplied by the volume of one

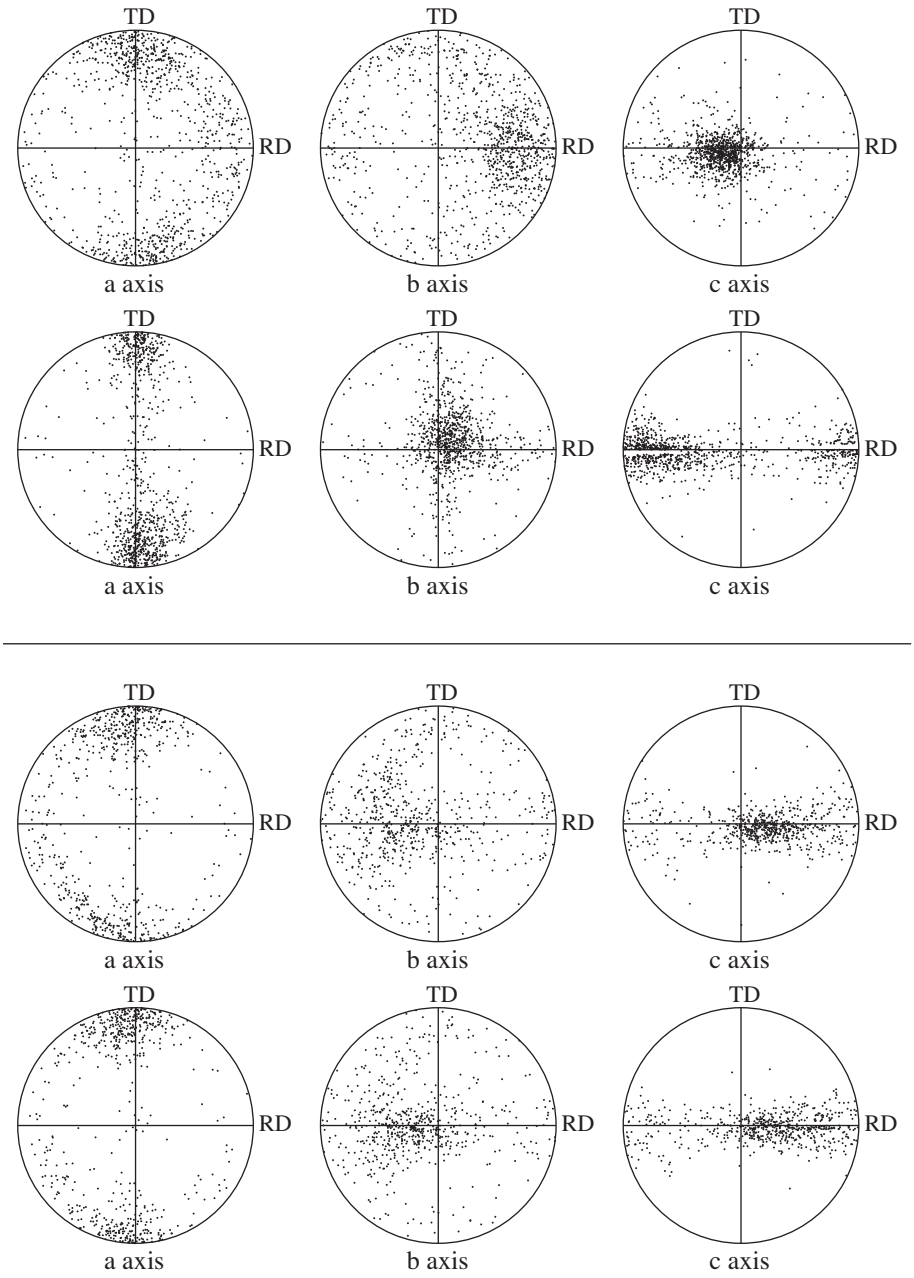

Fig. 7. Pole figures of the main axes of the equivalent ellipsoids for cells in the (RD,TD) plane in a PU580 sample (top) and a Ni580 sample (bottom) in their initial (first row) and deformed (second row) states.

voxel, which is 125 μm^3 at the resolution 5 μm. The volume of equivalent spheres whose diameters are 350, 580 and 1200 μm would be about 0.022, 0.102 and 0.905 mm^3, respectively. The difference with the volumes calculated by image analysis, respectively 0.021, 0.065 and 0.557 mm^3, indicates a better control of the manufacturing for the small pore sizes. We also calculated the diameter of an *equivalent* spherical pore whose volume would be equal to the mean cell volume. Thus the *real* pore sizes respectively are 344, 498 and 1021 μm. One can note that these *equivalent* diameters are actually close to the lengths of the *b* axis found to be 336, 496 and 990 μm in average. As a matter of fact, the lengths of the *c* axis in PU580 and PU1200 foams, respectively 611 and 1283 μm, are almost equal to the expected pore sizes whereas in PU350 the *c* axis is larger with 444 μm length. The inertia properties of the cells can be used to define three indicators of anisotropy, namely the ratios c/b, b/a, and c/a. We define the main foam anisotropy ratio as the largest one, namely c/a. The mean values of this ratio (respectively 1.52, 1.42 and 1.47) are somewhat larger than values reported by Montminy et al. (2004) and Jang et al. (2008) (respectively 1.292 and about 1.25). The difference is due to the method used in each case. The measure in Jang et al. (2008) is the ratio of the cell size in the rise direction over the one in the transverse direction. The measure in Montminy et al. (2004) consists in summing up separately the absolute values of all the *x*, all the *y* and all the *z* components of the vectors describing the ligaments of a cell, the anisotropy being the ratio of the largest sum over the smallest one.

To represent the distribution of cell orientation, the stereographic projection of the eigenvectors of the inertia tensors is adopted. The pole figures presented in Figs. 7 and 8 are the stereographic projections of the directions of the axes *a*, *b* and *c* in the plane (RD,TD). One might note a slight tilt of the general orienta-

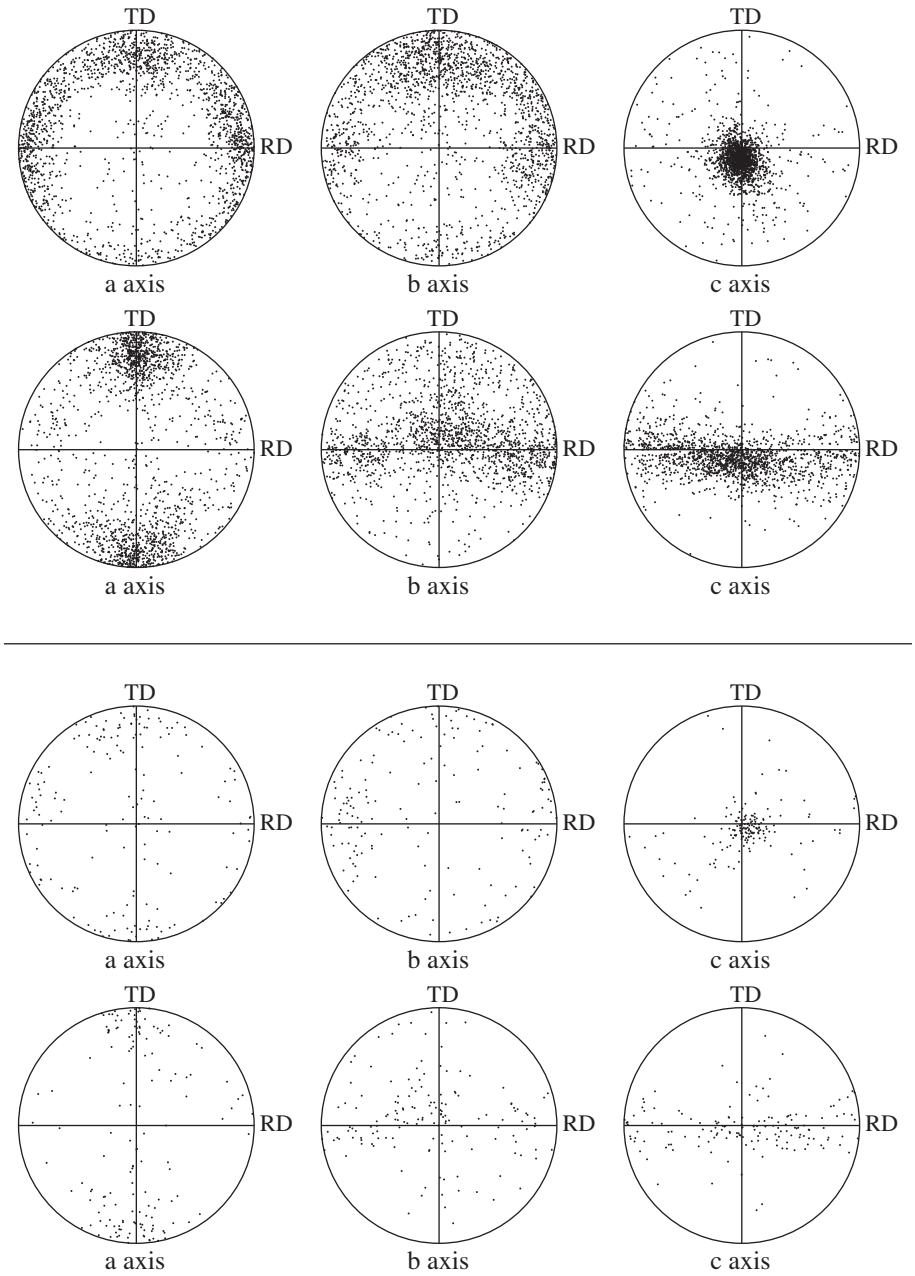

Fig. 8. Pole figures of the main axes of the equivalent ellipsoids for cells in the (RD,TD) plane in a PU350 sample (top) and a PU1200 sample (bottom) in their initial (first row) and deformed (second row) states.

tion given by these pole figures with respect to the (RD,TD,ND) frame. This deviation is due to the slight difference in orientation between the frame of the foam (RD,TD,ND) and the corresponding frame of the 3D image (z,x,y). In the PU foams the c axis is clearly oriented along ND. This is in agreement with the common observations in the literature: Pores are elongated in the *rise* direction. The axes a and b essentially remain contained but randomly distributed in the plane (RD,TD). This observation shows that the initial shape anisotropy of the PU foams is not between ND and TD but between ND and the plane (RD,TD).

The above description of the initial morphology of the PU foams is to be compared with the following description of the initial morphology of the Ni580 foam. The mean cell volume in the Ni580 is about 0.078 mm^3, which is about 20% smaller than the expected pore volume. This gives an equivalent cell diameter, i.e. a *real* pore size, of about 530 μm close to the 548 μm of the b axis length in the PU foams. The Ni580 shape anisotropy is about $c/a = 1.46$ which is in the same range as in the PU foams. The main difference between the PU580 and the Ni580 lies in the difference of cell orientation. In the Ni580 foam, the cells tend to be elongated along RD while the a axis displays a preference for TD and the b axis for ND.

This fact can be correlated to the load applied to the PU580 during the electroplating of the nickel, implying a deformation along RD which is the loading direction. Then, the anisotropy is significant between RD and TD with a second but weaker anisotropy between RD and ND. This represents an essential difference from the initial PU morphology.

Applying a pulling force along RD is necessary to ensure a continuous rolling of the PU foam sheet in the electroplating bath, the length of the sheet being too long for the bath dimensions. To assess the validity of this hypothesis of deformation induced change of morphology during processing, we will compare in the next

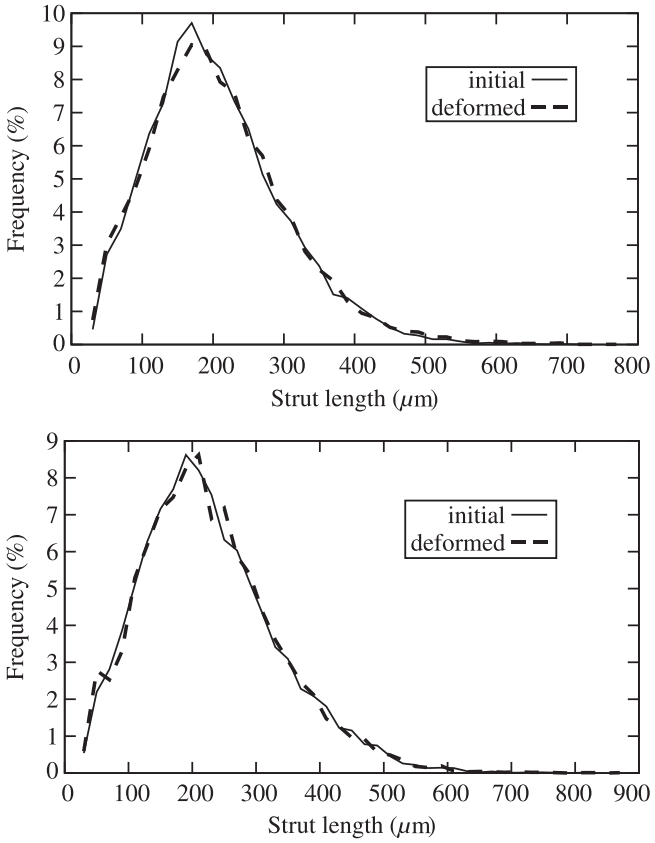

Fig. 9. Strut length distribution for a PU580 sample (top) and a Ni580 sample (bottom) in their initial and deformed states.

subsection the morphology of deformed PU foams and the initial morphology of nickel foams.

3.2. Evolution of cell orientation during deformation

Some PU580 foam samples were deformed up to 15% in the RD direction by means of *in situ* mechanical testing. Some Ni580 samples were deformed up to 3% which is lower than the fracture strain of 4% for nickel foam in tension along the RD direction according to Fig. 3.

In the deformed PU580 foams, the pole figures of Fig. 7 show that the *c* axis is oriented along the loading direction (RD), the *a* axis along TD and the *b* axis along ND. After 15%, the cells are therefore elongated along RD. This does not mean that the cells have rotated during deformation. It rather suggests that actually the initial *b* axis is stretched and becomes the main axis *c* in the deformed state. The Poisson effect reduces the length of the initial *c* axis which becomes *b* in the deformed state, the *a* axis remaining the smallest one.

The comparison of the pole figures for deformed PU580 and initial Ni580 in Fig. 7 shows that this deformed configuration of PU580 has common features with the initial configuration of Ni580. This confirms that the initial Ni580 state corresponds to a deformed state of the PU foam subjected to a load along RD. This state is then frozen by the electroplating of the nickel. However the alignment of the *c* axis with the direction RD is more pronounced in the PU580 foams than in the initial state of Ni580. This suggests that the straining of the PU foam during the nickel foam processing is less than 15% and estimated at 7–8%. The actual load in the process is hard to measure due to friction at different stages of the process.

Table 3
Evolution of the length of the 42 struts belonging to cell #1. Initial and final lengths and the corresponding strains are given in the format "experimental value/finite element value".

Initial length	Deformed	Strain (%)
L_{strut} (μm ± 5 μm)		
62/68	61/68	−1.8/0.2
98/99	95/99	−2.9/-0.1
103/104	104/105	0.5/1.0
113/108	110/108	−2.7/-0.8
114/116	118/117	4.1/0.9
114/118	115/118	0.3/-0.1
120/125	124/126	3.2/0.9
125/114	126/117	0.7/2.8
125/126	125/125	0.0/-0.8
133/136	133/139	0.2/2.2
135/133	138/137	2.5/3.2
139/148	141/154	1.6/4.0
148/157	151/160	2.1/1.7
160/160	166/173	3.8/7.7
161/158	156/158	−3.3/-0.0
167/170	174/181	4.1/6.4
169/167	175/178	3.6/6.9
173/172	182/176	4.9/2.4
176/180	179/180	1.5/-0.3
189/185	178/182	−5.9/-1.5
190/190	202/201	6.4/5.8
190/188	187/187	−1.8/-0.5
192/192	195/193	1.6/0.6
194/193	193/193	−0.5/0.1
194/198	200/197	3.3/-0.3
197/204	198/201	0.6/-1.1
206/212	194/215	−5.9/1.4
207/213	207/214	0.2/0.2
209/211	209/221	−0.1/4.5
210/203	221/220	5.3/8.3
220/212	236/229	7.2/7.7
227/218	225/217	−0.6/-0.4
237/234	227/233	−4.5/-0.3
237/232	234/242	−1.4/4.3
239/248	228/249	−4.8/0.4
241/235	234/234	−2.7/-0.6
246/241	252/260	2.4/7.7
251/243	249/254	−0.9/4.7
252/251	251/260	−0.7/3.5
270/269	268/277	−0.5/2.9
321/318	324/319	1.2/0.3
330/321	306/315	−7.3/-1.7
Mean values (μm ± 5 μm)		
186/186	186/189	0.4/2.3 ± 3.0/3.0

After only 3% straining, the evolution of the cell orientation in deformed Ni580 is barely visible. One might see that the *a* axis is getting closer to TD, the dots of the *b* axes are a bit more clustered about ND and the *c* axis is moving slightly along RD.

The cell deformation mechanisms in PU are confirmed by the observation of other pore sizes for which results are given in Fig. 8 in the initial and 15% strained states. The initial cell orientations of the PU350, PU580 and PU1200 are almost identical, with the *c* axis aligned with the ND direction and no preferred orientation for *a* and *b*. After 15% straining, the main axes *c* are distributed in the (RD,ND) plane, whereas the *a* axes are mainly aligned with TD. The clustering of *c*-axes along RD is found to be more pronounced for PU580 than for PU350 and PU1200.

3.3. Evolution of cell size and strut length during deformation

This subsection gives a quantitative description of the evolution of the geometrical characteristics of the cells during deformation. Figs. 5 and 6 compare the distributions of the size and volume of the individual cells in their initial and deformed states. Table 2 gives the main axes lengths, the main anisotropy ratio, the mean

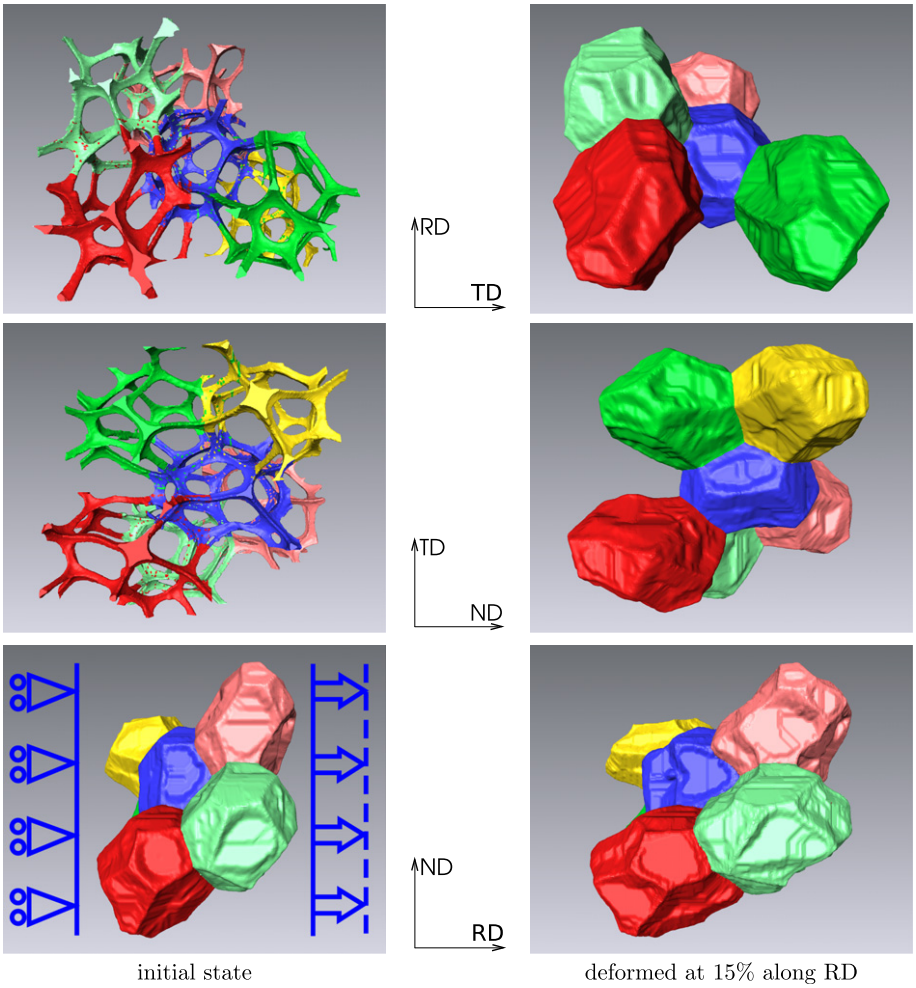

Fig. 10. Top and middle lines: group of six cells (left) extracted from the core of the PU580 sample and the corresponding packs of voxels (right) determined from the 3D segmentation procedure. The cells are shown according to two different views. Bottom line: Tensile conditions applied to the group of studied cells (left) and corresponding deformed state (right).

cell volume, equivalent sphere radius and mean strut length of all analyzed cells in the foam samples in their initial and deformed states.

The cell volume is reduced by about 5%, going down from 0.065 to 0.062 mm^3 in PU580, after 15% straining. In the Ni580, the cell volume remains essentially unchanged after 3% straining. This evolution implies a reduction of the equivalent pore size from 498 to 490 μm in PU580 while it remains at 530 μm in Ni580.

The lengths of the inertia axes are the geometrical characteristics which are the most sensitive to deformation. In PU580 the *a* axis length is eventually reduced from 431 to 395 μm (more than 8%) while the two others lengths increase from 496 to 503 μm (almost 1.5%) for *b* and from 611 to 629 μm (near 3%) for *c*. The same trend is observed in the Ni580 foam, but to a lesser extent. The *a* axis length decreases from 446 to 440 μm (about 1.3%) and the *b* axis length increases from 548 to 552 μm (less than 1%), the *c* axis remaining almost constant. The foam anisotropy ratio c/a follows the same trend for both PU580 and Ni580 during deformation, namely an increase, from 1.42 to 1.59 for PU580 and from 1.46 to 1.48 in Ni580.

Studying the deformation of an open-cell foam also means studying the deformation of the struts. Fig. 9 displays the histograms of the strut lengths for PU580 and Ni580 in their initial and deformed states. A striking feature of these results is that the strut length essentially does not change during the deformation of the foam for both PU and nickel foams. The values of the mean strut length are provided in Table 2: The mean length of the strut increases of 2 μm in both PU580 and N580 going up from 186 to 188 μm and from 205 to 207 μm, respectively. This increase remains below the precision of the measurement which is 5 μm at best.

These observations reveal that globally the strut lengths do not change during deformation at the considered strain levels. This does not mean that individual strut length do not change since the histograms provide results for all the struts without following each individual strut during deformation. For one single PU580 cell, we have followed 42 individual struts in their initial and final states. No automatic procedure has been designed so that the results have been determined for one single cell in Table 3. Some struts are indeed found to elongate up to 6% and other ones to shorten by 5%, but no average length change is found in this cell.

The previous observations suggest that strut stretching is not a significant deformation mechanism in the considered open-cell PU and nickel foams. Gong et al. (2005) consider that the strain energy in a strut is the sum of 4 contributions: tension–compression, bending, shear and torsion. The foams studied in the present work have struts with Plateau border cross sections whose torsional rigidity can be estimated by following the method by Warren et al. (1997). As mentioned by Gong et al. (2005), the torsional rigidity contribution to the strain energy can be neglected. The amount of cell shearing can be determined for individual cells from the micro-tomography data. This will be done and discussed in

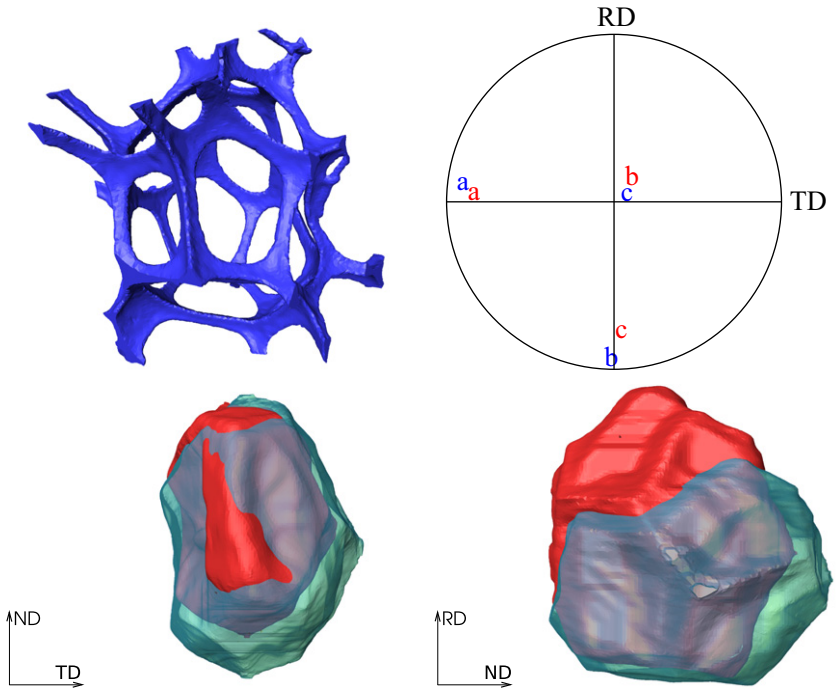

Fig. 11. Cell #1: (top left) 3D rendering of the central cell of the group; (top right) Orientation of the axes of the equivalent ellipsoid in the (RD,TD) plane in its initial (blue) and deformed (red) states; (bottom) 3D rendering of the equivalent pore in the planes (TD,ND) and (ND,RD) in its initial (transparent blue) and deformed (red) states (PU580 foam). (For interpretation of the references to colour in this figure legend, the reader is referred to the web version of this article.)

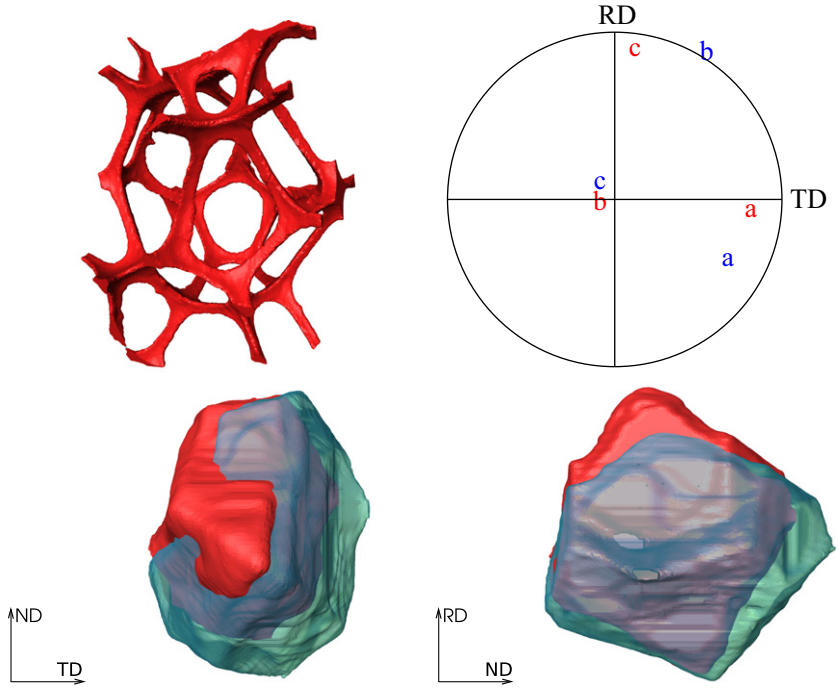

Fig. 12. Cell #2: (top left) 3D rendering of the central cell of the group; (top right) Orientation of the axes of the equivalent ellipsoid in the (RD,TD) plane in its initial (blue) and deformed (red) states; (bottom) 3D rendering of the equivalent pore in the planes (TD,ND) and (ND,RD) in its initial (transparent blue) and deformed (red) states (PU580 foam). (For interpretation of the references to colour in this figure legend, the reader is referred to the web version of this article.)

Section 4.2 for the PU foams. Alternative mechanisms are strut bending and complex node deformation. They cannot be evidenced quantitatively by the previous 3D image analysis techniques. We have not found any systematic way of detecting strut bending from the 3D images. We will rely on finite element simulations for identifying these mechanisms at work during straining of groups of cells.

3.4. Deformation of a group of cells

Texture evolutions and histograms of main axes and strut length provide global statistical information about the foam behavior. It is also useful to follow individual cells during deformation in order to detect deformation mechanisms. Systematic correlation analysis will be necessary in the future to systematically track a

large number of cells. The present analysis is limited to a group of six cells from the PU580 foam material.

The segmented images of the initial state of the six selected cells are shown in Fig. 10 according to two different views (top-left and middle-left). The 3D image analysis is used to fill the cells and obtain individual objects for which the inertia tensor can be computed. The initial and deformed filled cells can be seen in Fig. 10 (top-right and bottom-right). Another view of this group of cells is given in the bottom line of the same figure, that shows the elongation of the cells after 15% along the RD direction. In that way, the evolution of the inertia tensor can be followed for each individual cell, in contrast to what was done in Section 3.2 where cells were treated globally. In Figs. 11 and 12, the cells at the top left corner have the same color as in Fig. 10. The top right parts of Figs. 11 and 12 give the pole figures for the initial and deformed inertia tensor main axes for the cells #1 and #2 (blue and red cells, respectively). It appears that for both of them, the *c*-axis initially normal to the foam sheet finally lies along the RD direction. This trend was observed globally in Section 3.2, it is also observed for several individual cells. The *a* axes are essentially unchanged after deformation for both cells, whereas *b* and *c* are interchanged for both cells. The initial and final filled cell shapes are also compared at the bottom lines of Figs. 11 and 12 from two different viewpoints that underline individual cell elongation in the tensile direction and the cell contraction in the transverse plane. It can clearly be seen, in particular in cell #1, that the cell was initially elongated in the ND direction and that it then aligned in the RD direction.

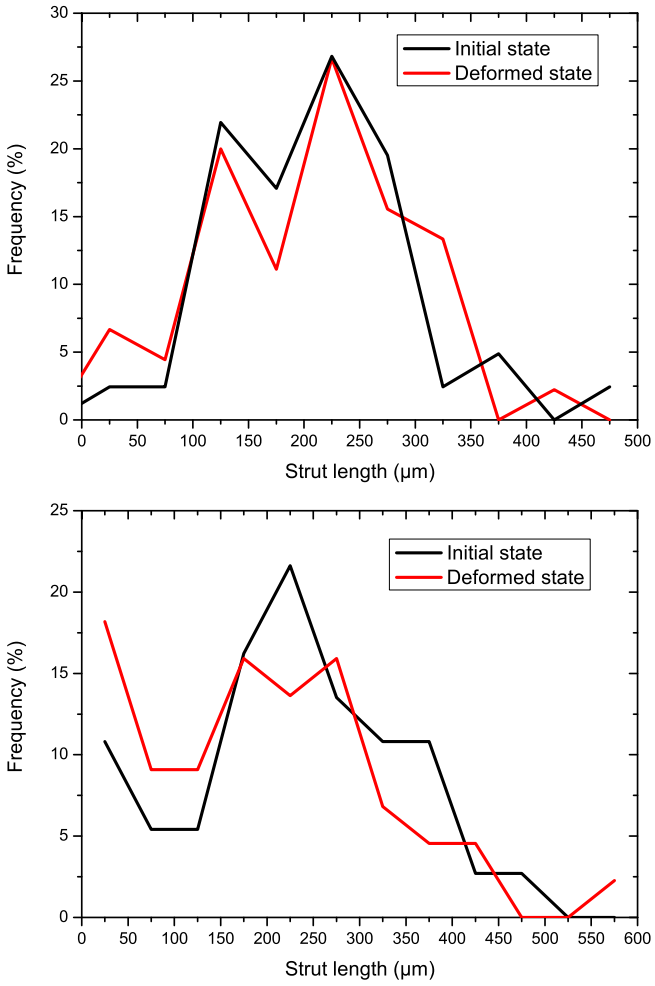

Fig. 13. Strut length distribution for cell #1 (top) and cell #2 (bottom) in their initial and deformed states (PU580 foam).

Accordingly, cell deformation is accompanied with a change in the hierarchy of inertia axes compared to the frame (RD, TD, ND).

Building the skeleton for each individual cell makes it possible to detect all the struts belonging to each cell and their corresponding lengths. The list of the initial and deformed length of the 42 struts of cell #1 is provided in Table 3. This information is available for the six cells of the considered group. Histograms of strut length can also be built for each cell. They are given for the cells #1 and #2 in Fig. 13. No significant evolution of the histogram was found for cell #1. This is also the case for cell #2 even though a slight trend for strut shortening is observed in this cell, see Fig. 13 (bottom).

4. Mechanical behavior of PU foam

The cell deformation mechanisms can be taken into account to predict the macroscopic foam response by means of microstructural finite element simulations that integrate the real morphology of foam volume elements. The quality of obtained images is sufficient to produce finite element meshes of individual cells and groups of cells following a computational strategy initiated by Cailletaud et al. (2003) for heterogeneous dense materials and Maire et al. (2003) for metallic foams.

4.1. Modeling the overall mechanical response

Two possible strategies follow from the performed image analyzes. The simplest one consists in starting from the obtained skeleton of the open cellular structure and building a beam network meshed by finite elements, procedure reviewed for instance in Kaoua et al. (2009) for nickel-based foams. Varying filled and hollow Plateau borders can be used as beam cross sections for PU and nickel foams, respectively. Similar strategy exists for closed-cell foams modeled as shell elements (Caty et al., 2008). As it was observed by Badiche et al. (2000), the considered struts are generally not slender enough to be regarded as beams. The slenderness is defined as the ratio between mean cross section size and strut length and it has the order of magnitude of 0.2. Also, the rather massive nodes connecting struts play a significant rôle in the foam deformation. A special constitutive model should be built for node connection in a realistic beam model for this type of foams, rather than usual rigid or free junction connections. The second possible strategy is to use 3D finite element meshes of the struts and cells. This is an extremely costly strategy that takes full account of the morphological information gained by X-ray micro-tomography. It also has the advantage that realistic non-linear constitutive equations can be used for the mechanical behavior of the constituent, namely PU on the one hand and pure nickel on the other hand. We have adopted this technique for PU and nickel foams and present the obtained results, necessarily limited to small number of cells due to the difficulty of building large 3D finite element meshes of real images.

The finite element mesh of PU foams is obtained by constructing first a 2D mesh of the foam surface as deduced by a marching cube algorithm from part of a 3D segmented tomography image, by means of the Avizo[1] software. Then the 3D mesh made of linear tetrahedra is produced by Avizo. The mesh must then be improved fulfilling geometrical element quality requirements and reduced in size. This is done with the program Yams developed at INRIA.[2] More details on systematic meshing of tomography images based on this series of softwares can be found in Madi et al. (2007). The final mesh is converted into quadratic tetrahedral elements with reduced integration.

[1] MERCURY Computer Systems – http://www.mc.com/.

[2] Inria: Institut National de Recherches en Informatique et en Automatique – http://www.inria.fr/.

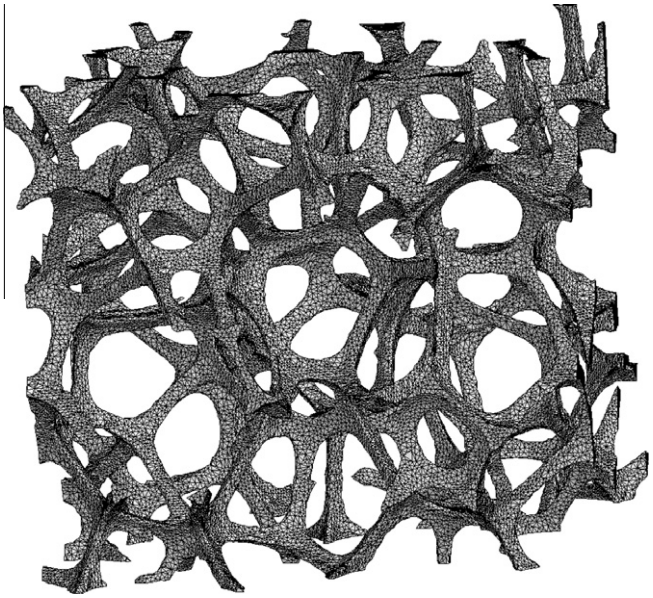

Fig. 14. Finite element mesh of a PU580 foam sample made of a single entire cell and parts of the first neighbors.

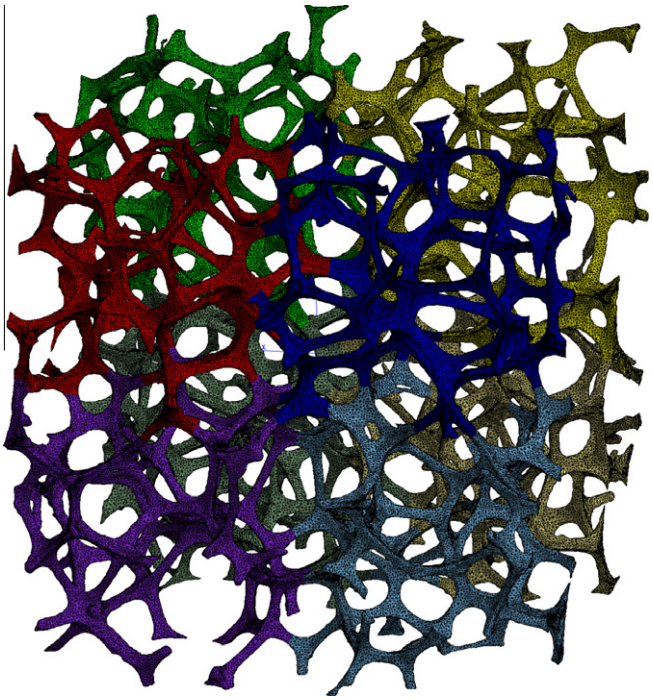

Fig. 15. Finite element mesh of a PU580 foam sample made of 24 complete or cut cells. The colors denote the sub-domains of the mesh used for parallel computing. (For interpretation of the references to colour in this figure legend, the reader is referred to the web version of this article.)

Two finite element meshes are considered in this work in Figs. 14 and 15. The first one contains one single entire PU cell, the cell #1 of Fig. 11 surrounded by its first incomplete neighboring cells. The second one contains 24 cells and corresponds to a larger zone of the foam centered around the cell #1. The first mesh is made of 105,000 nodes corresponding to 315,000 degrees of freedom[3] whereas the larger domain gives rise to 1.5 million of degrees of freedom.

We are interested in the mechanical behavior of the PU foam in the considered strain range [0,0.15]. Locally the PU material can reach higher strain levels but remains below 0.4, as it will turn out. A simple constitutive model is sufficient to account for the PU material, namely the compressible Mooney–Rivlin model (Ogden, 1984). The displacement vector is denoted by $\underline{\boldsymbol{u}}$ and $\underset{\sim}{\mathbf{F}}$ is the deformation gradient defined as:

$$\underset{\sim}{\boldsymbol{F}} := \underset{\sim}{\mathbf{1}} + \nabla \underline{\boldsymbol{u}}, \quad \underset{\sim}{\boldsymbol{C}} := \underset{\sim}{\boldsymbol{F}}^T \cdot \underset{\sim}{\boldsymbol{F}}, \quad \underset{\sim}{\boldsymbol{E}} := \frac{1}{2}(\underset{\sim}{\boldsymbol{C}} - \underset{\sim}{\mathbf{1}}) \tag{1}$$

with $\mathbf{1}$ the identity tensor, $\boldsymbol{C}$ the right Cauchy–Green tensor and $\boldsymbol{E}$ the Green–Lagrange strain tensor. The nabla operator is applied with respect to the Lagrange coordinates attached to the reference configuration. The three invariants of the right Cauchy–Green tensor are defined as:

$$I_1 := \operatorname{trace} \underset{\sim}{\boldsymbol{C}}, \quad I_2 := \frac{1}{2}(I_1^2 - \operatorname{trace}(\underset{\sim}{\boldsymbol{C}} \cdot \underset{\sim}{\boldsymbol{C}})), \quad I_3 := \det \underset{\sim}{\boldsymbol{C}} \tag{2}$$

The chosen strain energy potential is

$$W = \alpha(I_1 - 3) + \beta(I_2 - 3) + \frac{1}{2}\gamma(\alpha + \beta)(I_3 - 1)^2 \tag{3}$$

where α, β and γ are three material parameters. A high value $\gamma = 1000$ MPa is chosen that penalizes volume changes so that the material constituent is regarded as quasi-incompressible. The parameters α, β remain to be identified.

The mesh is contained in a cube box and boundary conditions must be applied to all the nodes lying on the faces of this cube. There is no unique way to apply a tensile loading on the considered volume elements. Homogeneous strain boundary conditions are known to deliver too stiff overall response when applied to volume elements smaller than the representative volume element (Kanit et al., 2003). In contrast, homogeneous stress based conditions may lead to a too soft material response. Periodic boundary conditions very often are the best-suited conditions to estimate the overall properties on finite size material volumes. They are however difficult to apply in the case of real images of materials when there is no mesh periodicity on opposite faces of the cube. That is why we have resorted to mixed homogeneous boundary conditions with prescribed displacements in the tensile direction for the nodes lying on the two faces perpendicular to the loading directions. The lateral faces are then left free of forces. The internal

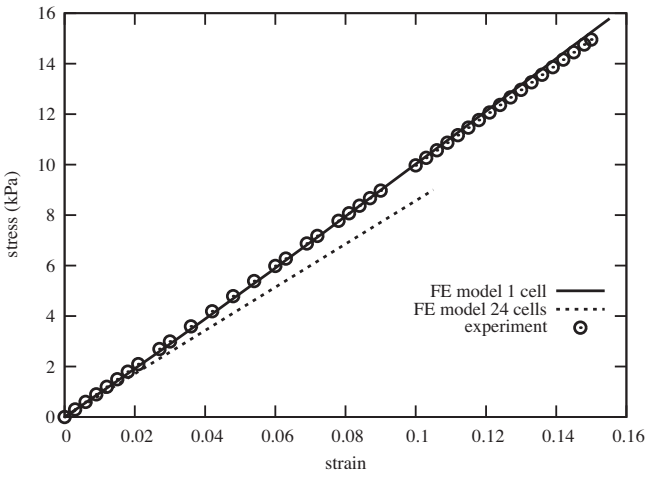

Fig. 16. Comparison between the experimental tensile curve of the PU580 foam and the predicted results from the finite element analyzes on the volume elements considered in Figs. 14 and 15.

[3] The degrees of freedom in the finite element model are the three displacement components of each node.

surface of the cells, lying inside the volume element, are also free of forces. The overall tension is prescribed along the RD direction. The foam response is expected to be quasi-isotropic in the (RD, TD) plane since no preferred in-plane orientation of the cells was found.

Parallel computing was used to obtain the results in a reasonable time based on the domain decomposition methods with domains shown in color in Fig. 15.

Fig. 16 compares the experimental and finite element stress strain curves for the foam. The plotted stress is the ratio of the total applied force divided by the initial cross-section of the cube containing the foam and corresponds to the first component of the first Piola–Kirchhoff stress tensor. The plotted strain is the relative displacement in the tensile direction divided by the initial length, i.e. the component $F_{11} - 1$. In the investigated strain range, the relationship between the first Piola–Kirchhoff stress and the deformation gradient component turns out to be quasi-linear both experimentally and numerically. The smaller volume containing one single cell and its first neighbors provides a slightly stiffer response than the 24-cell volume element. The modulus $\beta = 3.9$ MPa (keeping α close to 0) has been identified by comparing the finite element prediction for the single cell mesh and the experimental curve. Both computed overall stress–strain curves are close to the experimental results showing that the local PU constituent behavior is close to the actual one and that the considered volumes are not far from being representative for the determination of hyperelastic behavior within the considered strain range.

The found parameter values are comparable to typical ones for Mooney–Rivlin models in bulk PU, as found for example in the reference Laiarinandrasana et al. (2003). There are many sorts of PU with strongly different stiffnesses so that only the order of magnitude is relevant here for comparison. Differences may exist between the mechanical behavior of PU as bulk material or in cell walls of a foam. Micromechanical tensile experiments on individual PU struts could be imagined, complemented by microindentation tests, for an improved PU material characterization.

4.2. Quantitative analysis of individual cell deformation

The finite element results also give information about the local strains in the struts and nodes of the considered group of cells. Fig. 17 shows the field of equivalent Green–Lagrange strain, defined as $E_{eq} = \sqrt{E_{ij}E_{ij}}$, inside the cell #1, i.e. the central cell of the mesh of Fig. 14 at three different strain levels. This field is complex in the sense that local straining essentially starts at stress concentrators close to strut junctions and finally invades several entire

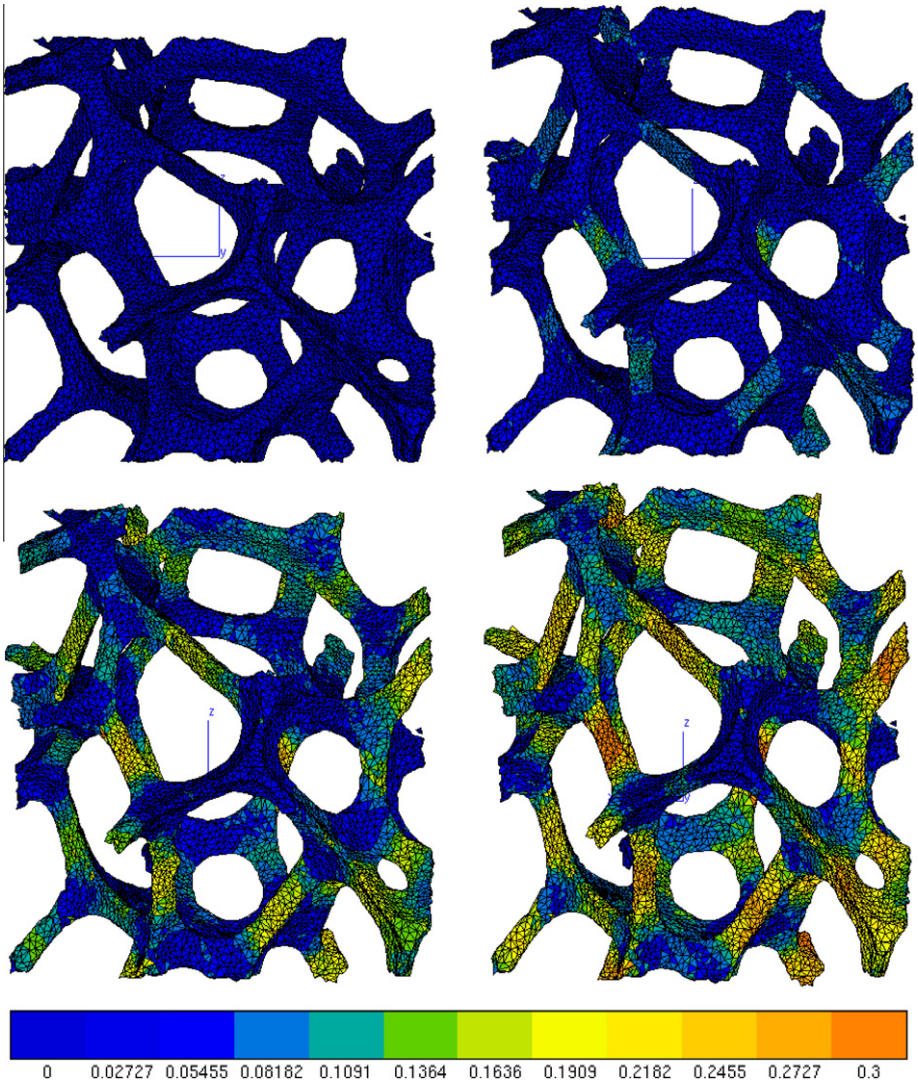

Fig. 17. Finite element mesh (top left) and equivalent Green–Lagrange strain in the cell struts of the central cell of Fig. 14, at the overall tensile strain levels of 0.05, 0.10 and 0.15, respectively top right, bottom left and bottom right pictures. Tensile direction is vertical.

struts. Intense shear can be observed in the short strut in the middle left of the picture. Although an overall strain of 15% is applied, local strain values can be greater than 30%. In at least two visible struts, the middle part of the beam is intensely strained whereas the two associated nodes are less deformed.

The 3D image analysis technique used to obtain the skeleton of each cell from micro-tomography images has provided the positions of the junctions of the struts in this initial and deformed images. We have determined the node of the finite element mesh which is the closest to each junction in the initial configuration. There is some error in the determination of these nodes because junctions are hollow and that the determined image junction voxel may lie in the hollow part of the junction. In the latter case, we select the closest finite element node lying on the nickel surface mesh. The displacements of these special nodes allow us to construct the deformed skeleton of the considered group of cell from the finite element analysis. The initial and final skeletons of all complete cells out of the 24 cells of the mesh of Fig. 15 are shown in Fig. 18, from the micro-tomography analysis. Direct comparison is drawn in Fig. 19 between the experimental and computed final deformed states of the single central cell #1 of the mesh of Fig. 14. In particular, we can compare the initial and final strut lengths in this cell. The experimental and numerical values are given in Table 3. The finite element results confirm the experimental fact that both positive (tensile) and negative (compression) elongations of struts are observed inside the cells and that the corresponding strain values are significantly smaller that the applied overall strain of 15%. A good correspondence is found between finite element and experimental results for individual struts and in average, despite the fact that the determination of strut length from the nodes of the skeleton remains an idealized definition.

We can also define a deformation tensor for each individual cell, called here *micro-deformation* tensor, by interpolation of the displacements of all the corners of the skeleton of the considered cell. The cell micro-deformation tensor $\underset{\sim}{\boldsymbol{\chi}}$ and the translation vector $\underline{\boldsymbol{c}}$ are obtained by linear optimization of the system of N equations relating the coordinates of the initial positions $\underline{\boldsymbol{X}}^i$ to the coordinates of the final positions $\underline{\boldsymbol{x}}^i$ of the N nodes of each considered foam cell:

$$\underline{\boldsymbol{x}}^i = \underset{\sim}{\boldsymbol{\chi}} \cdot \underline{\boldsymbol{X}}^i + \underline{\boldsymbol{c}}, \quad 1 \leqslant i \leqslant N \tag{4}$$

The micro-deformation tensor can be split into a stretch tensor $\underset{\sim}{\boldsymbol{U}}^{\chi}$ and a rotation tensor $\underset{\sim}{\boldsymbol{R}}^{\chi}$ by means of the polar decomposition:

$$\underset{\sim}{\boldsymbol{\chi}} = \underset{\sim}{\boldsymbol{R}}^{\chi} \cdot \underset{\sim}{\mathbf{U}}^{\chi} \tag{5}$$

The components of these tensors are listed for six cells in Table 4 which correspond to the six cells studied in Fig. 10. The stretch tensor $\underset{\sim}{\mathbf{U}}^{\chi}$ displays shear components values that do not exceed 3%. The cell rotation is found to be very limited.

We can also define a geometric deformation tensor for each cell as the tensor that transforms the initial inertia tensor into the inertia tensor of the deformed cell. This deformation of the inertia tensor is not a material deformation since inertia eigenvectors are not material vectors. The stretch part of the inertia deformation tensor of each cell, called $\underset{\sim}{\boldsymbol{U}}^{\chi}_{inertia}$ in Table 4, is expected to be close to the micro-deformation tensor $\underset{\sim}{\boldsymbol{\chi}}$ when the material is homogeneously deformed, unless an interchange between the main axes takes place. Indeed, the inertia deformation tensor is found to be close to the micro-deformation tensor except for Cell #6.

The micro-deformation of each cell must be compared to the macro-deformation of the sample. The macro-deformation of the material zone analyzed by X-ray tomography was determined by selecting a large parallelepipedic zone containing the investigated

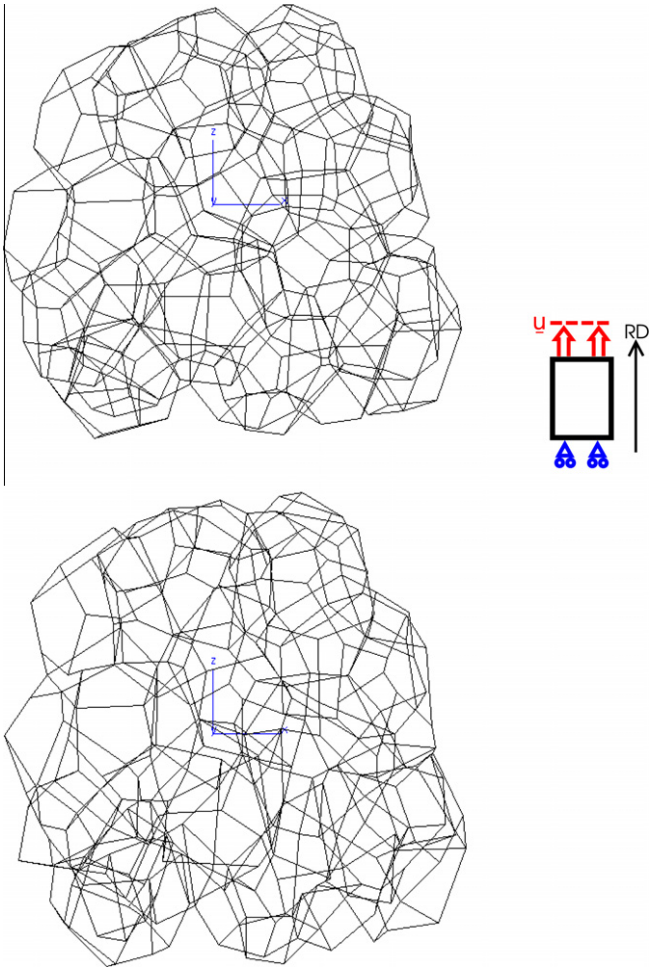

Fig. 18. Skeleton of a group of 11 closed cells extracted from the same zone of PU580 as that used for the mesh of Fig. 15. The top figure gives the initial foam morphology. The bottom figure provides the deformed state in vertical tension.

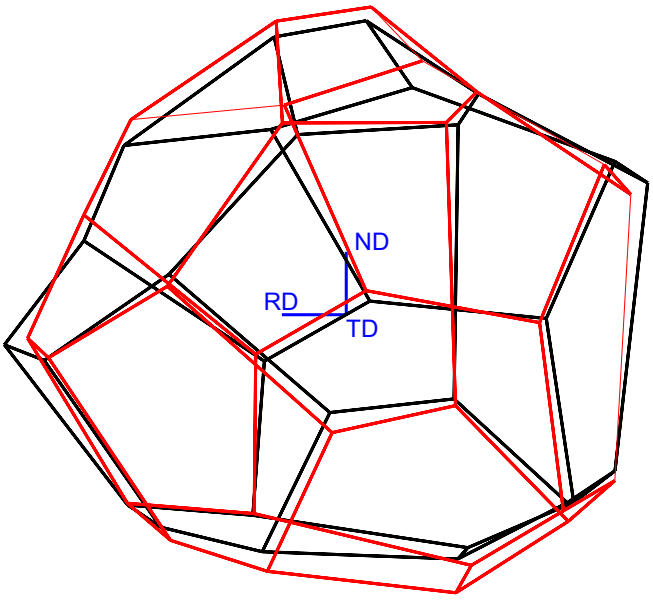

Fig. 19. Comparison between the superimposed deformed skeletons of the PU580 central cell #1 of Fig. 14 from the experimental and computational results.

Table 4
Inertia, micro-deformation and rotation tensors and translation vector for six cells in a PU580 foam sample in tension along RD. The components of the matrices are given with respect to the (RD,TD,ND) basis.

Number	$\underset{\sim}{U}^{\chi}_{inertia}$	Micro-deformation $\underset{\sim}{U}^{\chi}_{node}$	Rotation $\underset{\sim}{R}^{\chi}_{node} = \underset{\sim}{\chi}\cdot\underset{\sim}{U}^{\chi}_{node}$	Translation $\underline{c}$
Cell 1	$\begin{pmatrix} 1.246 & 0.022 & -0.007 \\ 0.022 & 0.874 & 0.001 \\ -0.007 & 0.001 & 0.888 \end{pmatrix}$	$\begin{pmatrix} 1.178 & 0.007 & -0.024 \\ 0.007 & 0.904 & 0.015 \\ -0.024 & 0.015 & 0.898 \end{pmatrix}$	$\begin{pmatrix} 0.999 & 0.010 & 0.033 \\ -0.011 & 1.000 & 0.017 \\ -0.033 & -0.018 & 0.999 \end{pmatrix}$	$\begin{pmatrix} 0.641 \\ 1.895 \\ 2.019 \end{pmatrix}$
Cell 2	$\begin{pmatrix} 1.020 & 0.045 & -0.006 \\ 0.045 & 0.974 & -0.023 \\ -0.006 & -0.023 & 1.008 \end{pmatrix}$	$\begin{pmatrix} 1.137 & 0.025 & -0.026 \\ 0.025 & 0.917 & -0.023 \\ -0.026 & -0.023 & 0.898 \end{pmatrix}$	$\begin{pmatrix} 1.000 & 0.010 & 0.000 \\ -0.010 & 1.000 & -0.006 \\ -0.000 & 0.006 & 1.000 \end{pmatrix}$	$\begin{pmatrix} 0.022 \\ 1.642 \\ 1.635 \end{pmatrix}$
Cell 3	$\begin{pmatrix} 1.147 & 0.105 & -0.007 \\ 0.105 & 0.940 & -0.001 \\ -0.007 & -0.001 & 0.892 \end{pmatrix}$	$\begin{pmatrix} 1.146 & -0.002 & -0.003 \\ -0.002 & 0.896 & 0.006 \\ -0.003 & 0.006 & 0.922 \end{pmatrix}$	$\begin{pmatrix} 0.999 & 0.032 & 0.016 \\ -0.032 & 1.000 & -0.005 \\ -0.016 & 0.005 & 1.000 \end{pmatrix}$	$\begin{pmatrix} 0.682 \\ 1.395 \\ 2.037 \end{pmatrix}$
Cell 4	$\begin{pmatrix} 1.131 & -0.021 & -0.183 \\ -0.021 & 0.896 & -0.023 \\ -0.183 & -0.023 & 0.936 \end{pmatrix}$	$\begin{pmatrix} 1.127 & 0.018 & 0.013 \\ 0.018 & 0.911 & 0.002 \\ 0.013 & 0.002 & 0.873 \end{pmatrix}$	$\begin{pmatrix} 0.999 & 0.035 & 0.006 \\ -0.035 & 0.999 & 0.019 \\ -0.006 & -0.019 & 1.000 \end{pmatrix}$	$\begin{pmatrix} 1.974 \\ 0.521 \\ 2.005 \end{pmatrix}$
Cell 5	$\begin{pmatrix} 1.208 & -0.019 & -0.133 \\ -0.019 & 0.920 & 0.014 \\ -0.133 & 0.014 & 0.893 \end{pmatrix}$	$\begin{pmatrix} 1.149 & 0.003 & 0.001 \\ 0.003 & 0.933 & 0.001 \\ 0.001 & 0.001 & 0.898 \end{pmatrix}$	$\begin{pmatrix} 1.000 & 0.001 & -0.010 \\ -0.001 & 1.000 & 0.022 \\ 0.010 & -0.022 & 1.000 \end{pmatrix}$	$\begin{pmatrix} 1.925 \\ 1.103 \\ 1.613 \end{pmatrix}$
Cell 6	$\begin{pmatrix} 1.010 & 0.017 & -0.001 \\ 0.017 & 1.011 & 0.039 \\ -0.001 & 0.039 & 0.966 \end{pmatrix}$	$\begin{pmatrix} 1.175 & 0.013 & 0.004 \\ 0.013 & 0.923 & 0.003 \\ 0.004 & 0.003 & 0.900 \end{pmatrix}$	$\begin{pmatrix} 1.000 & 0.025 & 0.014 \\ -0.025 & 0.999 & 0.031 \\ -0.013 & -0.031 & 0.999 \end{pmatrix}$	$\begin{pmatrix} 0.137 \\ 2.538 \\ 1.555 \end{pmatrix}$

six cells and by comparing the dimensions of the initial and final box sizes. The elongation of this zone coincides with the 0.15 straining applied to the sample but we also estimate the lateral contractions along TD and ND. We find:

$$\underset{\sim}{F}_{macro} = \begin{bmatrix} 1+\varepsilon & & \\ & 1-\nu_{TD}\varepsilon & \\ & & 1-\nu_{ND}\varepsilon \end{bmatrix} = \begin{bmatrix} 1.150 & & \\ & 0.957 & \\ & & 0.962 \end{bmatrix} \tag{6}$$

The components are given in the coordinate frame (RD,TD,ND). We can define two corresponding "Poisson ratios", $\nu_{TD} = 0.29$ and $\nu_{ND} = 0.25$ which are very close in spite of the initial cell elongation along ND. The comparison of the micro-deformation tensors from the Table 4 and Eq. (6) shows that the axial strain varies in the six cells from 0.13 to 0.18 around the prescribed strain $\varepsilon = 0.15$. The cell contractions, as determined from the microdeformation of the skeleton, are larger and slightly more anisotropic than the macroscopic ones. The ratio ν_{TD} varies from 0.44 to 0.7. The ratio ν_{ND} varies from 0.5 to 0.85. Contrary to the macroscopic case, the cell micro-deformations are such that $\nu_{ND} > \nu_{TD}$. Precision does not seem to be sufficient to conclude on local contraction values but what can be said is that both lateral contractions remain close.

The stretching and rotation of cells in a foam can be interpreted as additional microstructure information that can be incorporated in more general continuum theories, thus incorporating intrinsic length scales in the continuum modeling. The rotation of cells, which differs from the overall material rotation under non homogeneous loading conditions, can be interpreted as the additional degrees of freedom of the Cosserat model by Tekoglu and Onck (2008). The total microdeformation of cells itself can be regarded as a full set of additional degrees of freedom in a micromorphic theory, as done in Dillard et al. (2006). However, the properties of the latter generalized continuum models were not identified from actual micro-deformation or micro-rotation of cells, as determined in the present work.

5. Mechanical behavior of nickel foams

The computational strategy presented in the previous section for the determination of the mechanical response from the constitutive behavior of the constituent and the exact morphology of a group of cells, is now applied to the prediction of the behavior of the Ni450 nickel foam. The foam Ni450 is the only one for which we had micro-tomography images at a resolution of 1.24 μm, which is necessary for building a mesh of the walls of the hollow struts. Such a fine resolution was not needed for the PU foams. This resolution also limits the size of the considered images and the resulting final meshes.

5.1. Nickel strut constitutive behavior

The constitutive behavior of nickel making the walls of the hollow struts in the nickel foams strongly depends on the grain size and purity of the material. We were able to produce recrystallized nickel foils of high purity having the same bamboo grain microstructure and crystallographic texture as the *in situ* nickel material. This has been explained in details in Goussery et al. (2004). The nickel foils also had the same typical thickness as in the foam. Tensile tests were performed showing that the nickel foils display a linear elastic regime followed by a short non-linear domain and finally a long linear hardening regime until fracture occurs, quite abruptly (Dillard et al., 2006). This local behavior is adequately described by a standard J_2 plasticity model based on the von Mises yield function:

$$f(\underset{\sim}{\sigma}, R) = J_2(\underset{\sim}{\sigma}) - R \tag{7}$$

where $J_2(\underset{\sim}{\sigma}) = \sqrt{\frac{3}{2}\underset{\sim}{\sigma}^{dev} : \underset{\sim}{\sigma}^{dev}}$ is the von Mises equivalent stress and R is the isotropic hardening variable. The deviatoric part of the stress tensor is $\underset{\sim}{\sigma}^{dev}$. The model is formulated within the small strain framework, which is sufficient for the considered strain ranges for the nickel foam. The total strain tensor is split into its elastic and plastic parts:

$$\underset{\sim}{\varepsilon} = \underset{\sim}{\varepsilon}^{e} + \underset{\sim}{\varepsilon}^{p}, \quad \underset{\sim}{\sigma} = \lambda(\mathrm{trace}\,\underset{\sim}{\varepsilon}^{e})\,\underset{\sim}{1} + 2\mu\underset{\sim}{\varepsilon}^{e} \tag{8}$$

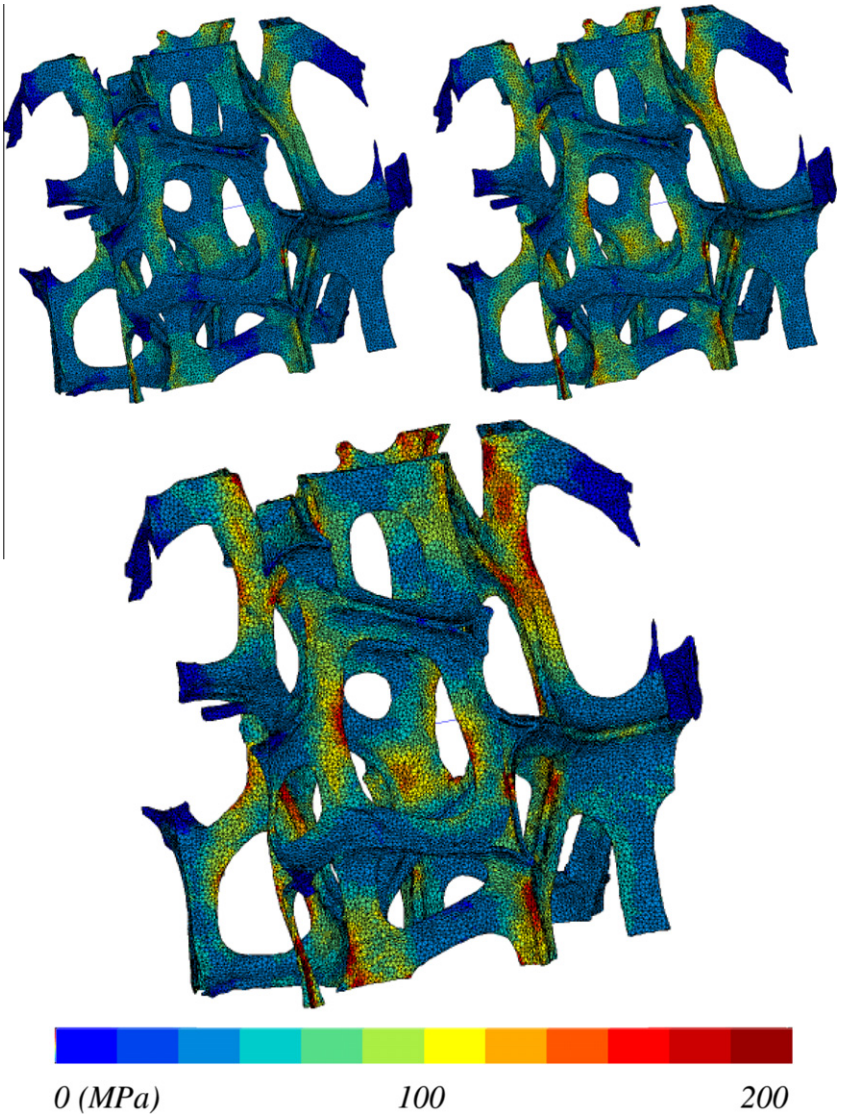

Fig. 20. Equivalent von Mises stress field in a Ni450 single cell after 0.04 (top left), 0.07 (top right) and 0.1 (bottom) tensile straining in the RD direction.

The stress is given by the isotropic linear elasticity law. The Young's modulus of pure nickel is taken to be $E = 204{,}000$ MPa and $\nu = 0.3$, and λ, μ are the corresponding Lamé constants. The plastic strain rate is obtained from the normality rule:

$$\dot{\underset{\sim}{\varepsilon}}^p = \dot{p}\frac{\partial f}{\partial \underset{\sim}{\boldsymbol{\sigma}}} \tag{9}$$

The cumulative plastic strain p is derived from the consistency condition and is such that

$$\dot{p} = \sqrt{\frac{2}{3}\dot{\underset{\sim}{\varepsilon}}^p : \dot{\underset{\sim}{\varepsilon}}^p} \tag{10}$$

The chosen evolution law for the hardening variable is

$$R = R_0 + Hp, \quad \text{with } R_0 = 84 \text{ MPa}, H = 1800 \text{ MPa} \tag{11}$$

where R_0 is the initial yield stress and H is the linear hardening modulus.

5.2. Representative volume element size

We consider first the finite element mesh of one single cell from a micro-tomographic image of Ni450, as shown in Fig. 20 and made of quadratic tetrahedra. The mesh takes into account a detailed description of the walls of the hollow struts and the complex geometry of the strut junctions. This leads to significantly more degrees of freedom than for the PU foam. In the computations presented in this section, the mesh size was chosen as a compromise between convergence of the global and local responses and the computational cost. The effect of changing the mesh refinement from 300,000 degrees of freedom to more than one million is shown in Fig. 21(a). The mesh is contained in a cube so that mixed homogeneous boundary conditions can be applied to the faces of the cube in order to prescribe tensile loading in average. The simulations have been performed for tension along the directions RD and TD. Fig. 20 shows the evolution of the equivalent von Mises stress field inside the cell during straining. It clearly indicates the strut junctions as main stress concentrators. The overall loading curves are given in Fig. 21(b) and compared to the experimental tensile curves. The elastic range is poorly described for both tensile directions. The predicted overall elastic stiffness is almost twice higher than the experimental one for each loading direction. It has already been noticed for several metallic foams that the effective stiffness is overestimated by such full-field analyzes (Caty et al., 2008; Burteau et al., 2008). In the contribution by Caty et al. (2008), a possible reason for the overestimation was attributed

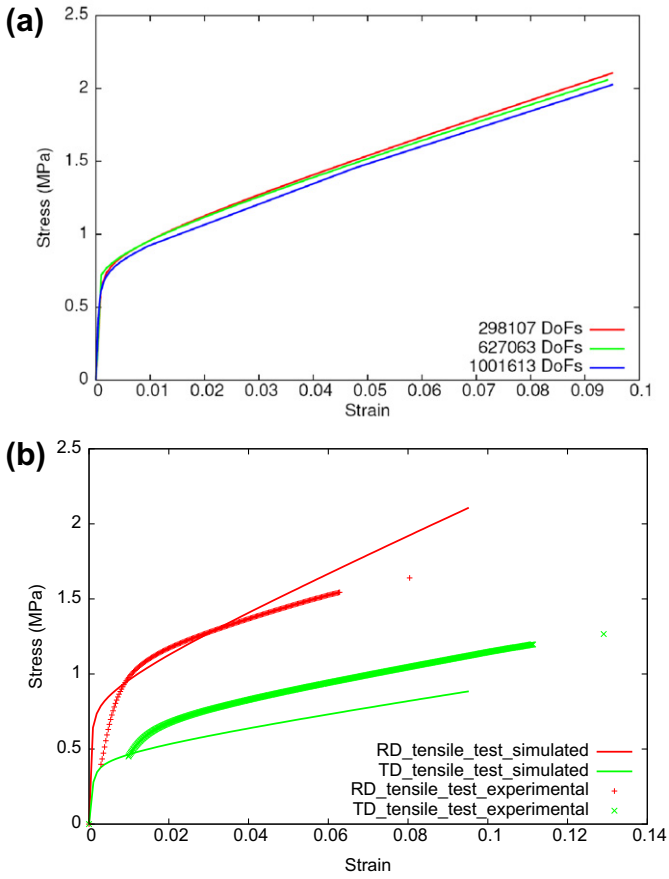

Fig. 21. Mesh sensitivity analysis on the single cell model of Fig. 20. (b) Experimental vs. simulated overall tensile curves for Ni450 in RD and TD directions.

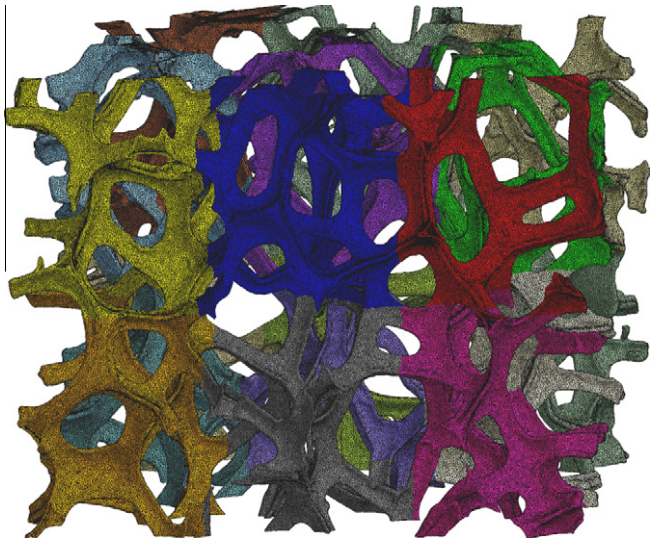

Fig. 22. 3D finite element mesh of a eight cell volume element of the Ni450 material.

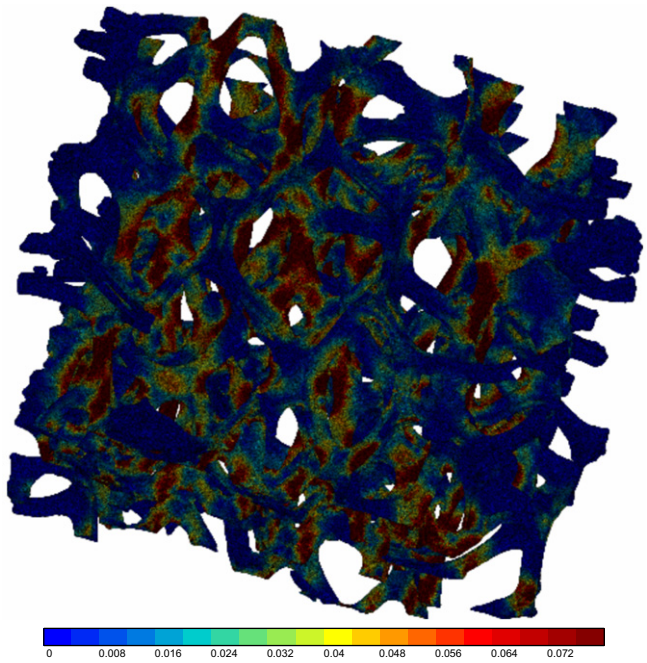

Fig. 23. Cumulative plastic strain field p in the Ni450 volume element of Fig. 22 after 0.05 overall straining.

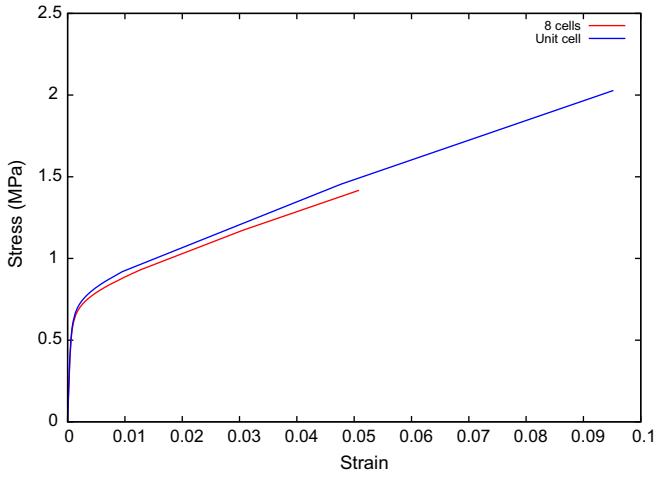

Fig. 24. Overall tensile curve for the tension of the Ni450 eight cell volume element of Fig. 22 and comparison with the response of the single cell model of Fig. 20. Tension is applied along the RD direction.

to porosity in the constitutive material and other defects. This is not the case for the nickel foam for which nickel is dense due to the electroplating followed by heat treatment. One possible reason is the lack of representativity of such a small unit cell. A larger volume element will be considered in the next paragraph but it leads to the same overestimated moduli. It may be that even larger volume elements are needed for the representativity of elastic properties, as pointed out by Kanit et al. (2003). In contrast, the anisotropy ratio between the apparent moduli in the RD and TD directions is correctly estimated by the finite element simulation: $E_{RD}/E_{TD} = 3$ according to the finite element simulations and $E_{RD}/E_{TD} = 2$ in the experiment. The stress level in the plastic regime is accurately predicted by the finite element model. The hardening moduli are also satisfactorily reproduced, especially in the TD direction. Importantly, the strong anisotropy is recovered by the one-cell model. This anisotropy of the mechanical behavior of the nickel foam is entirely due to the anisotropy of cell shape since, in the model, the constitutive response of pure nickel is isotropic. Although the response of the constituent was assumed to be essentially bi-linear, a non-linear overall hardening is obtained for the overall behavior due to the early plastic yielding in some parts of the cell and the spreading plastic zone. This short non-linear

regime is followed by extensive linear hardening, as observed in the experiment.

The huge mesh of Fig. 22 contains eight entire cells. It has been constructed to explore the representativity of the considered volumes of nickel foam. It requires 3.5 million of degrees of freedom to be determined according to the finite element method. The difficulty of constructing such huge meshes from the 3D micro-tomography images prevented us to consider larger or more numerous volumes. The plastic strain field inside this volume is shown in Fig. 23. At an overall strain level of 0.05, the plastic strain can be larger that 0.07 in some struts and some junctions. In a large part of the foam, the strain remains below 0.01. The corresponding overall stress–strain curve is given in Fig. 24. The response is slightly softer than the one found for the single unit cell. This result suggests that representativity for the plastic properties is reached even for small volume elements, although we have not been able to construct larger meshes.

6. Conclusions

The main findings of this work are the following:

1. The strong anisotropy of the mechanical behavior of nickel foams in the (RD,TD) plane is due to the anisotropic shape of the cells. The cell anisotropy was quantitatively and statistically characterized by means of X-ray micro-tomography. The plastic behavior characterized by the hardening modulus and anisotropic stress response is satisfactorily reproduced by the large scale finite element simulations.
2. The cell anisotropy is induced by deformation during the processing of the nickel foam. The foaming of the PU sets the initial morphology: The cells are elongated along the *rise* direction without any preferential orientation in the perpendicular plane. The morphology of the nickel foam does not conform to expectations: The elongation of the cells tends to be along the loading direction (RD) while the anisotropy seems to be between RD and TD. The morphology of the same PU foam but deformed up to 15% reveals that the cells are clearly elongated along RD while the strongest anisotropy appears to be between RD and TD. This indicates that the nickel foam has been deformed by less than 15% along RD, during processing. Tension is applied during the electroplating and heat treatment steps of the material processing. It results in the observed cell deformation.
3. Intensive finite element simulations were performed for both PU and nickel foams starting from the real morphology of cells. They provide satisfactory estimates of the effective foam behavior, especially of the induced mechanical anisotropy.
4. The statistical analysis of images and the finite element simulations give insight in the deformation mechanisms of PU and nickel foams. Strut stretching is not the major deformation mechanism since, in the mean, strut length is not significantly changed compared to the 0.15 strain applied to the PU foam, and the 0.03 applied to the nickel foam. As a matter of fact, bending, shear and complex deformation of junctions all contribute to the overall deformation, as illustrated by the maps of elastic or plastic strains predicted by the finite element approach. This statement may be different if significantly larger strain levels were to be applied to the PU foam.
5. Some elements of response have been provided to the question of representative volume element size for the mechanical properties of cellular solids which is a long-standing question of the mechanics of porous materials. The advantage of considering exact foam morphologies is that the predicted behavior is only dependent on volume size and of the dense material constitutive model and can be directly compared to the experimental overall curves. The striking results presented in this work show that small volume elements containing one main cell or up to 24 cells already provide fair estimates of the overall response of elastic–plastic metal foams, including stress level, hardening modulus and anisotropy, but also of the hyperelastic PU foams. The latter results should be extended to larger strain levels. This is not the case for nickel foam linear elasticity which is poorly predicted by the considered volumes. The dependence of representative volume element size on the type of mechanical properties has already been discussed at several places (Kanit et al., 2003).

The powerful computational strategy proposed in this work starts from systematic X-ray tomography and is followed by large scale finite element analysis. It is considered as an essential tool for the optimization of material properties and corresponding design of new morphologies (Bouaziz et al., 2008; Fullwood et al., 2010). The applied tension during material processing is needed for the line production and final coiling. We propose to use the applied tension on purpose to control the final anisotropy of cell shape and mechanical behavior. In that way, optimization of the nickel foam morphology is possible for target properties regarding anisotropy, ductility and pore size and shape requirements. Typical load to be applied in relation with the obtained anisotropy can be inferred from the presented results.

Such a design by cell deformation of nickel foams should be considered in a systematic way for battery and other recent applications like Diesel Particulate Filters (DPF). The latter is a promising future application of nickel based foams where gradual pore size and shape can be controlled for filtering particles of decreasing size while keeping sufficiently low pressure drops (Duchamp et al., 2007). This can be achieved by stacking foam sheets of different pore sizes and shapes. However, nickel cannot be used for high temperature applications because of oxidation. A powder technology has been used by Walther et al. (2008) to obtain a nickel base superalloy foam starting from the large porosity nickel foams studied in the present work. The obtained material can be characterized in tension but it must also withstand creep deformation (Oppenheimer and Dunand, 2007). Pore size and strut geometry can also be optimized for creep properties (Boonyongmaneerat and Dunand, 2009).

The computational method could also be used to investigate the multiaxial behavior of polymer and metal foams since complex loading conditions can be applied more easily than experimentally (Combaz et al., 2011). The ductile damage of the struts and nodes represents the next step in the computational approach. Fracture initiation has already been the subject of computational analysis in the 2D case and from the experimental point of view (Fazekas et al., 2002; Dillard et al., 2006; Amsterdam et al., 2008; Mangipudi and Onck, 2011), and in the full 3D case based on coupled micro-tomography and finite element for closed-cell foams (Youssef et al., 2005; Adrien et al., 2007).

References

Adrien, J., Maire, E., Gimenez, N., Sauvant-Moynot, V., 2007. Experimental study of the compression behaviour of syntactic foams by in situ X-ray tomography. Acta Materialia 53, 1667–1679.

Aly, M.S., 2010. Tensile properties of open-cell nickel foams. Materials and Design 31, 2237–2240.

Amsterdam, E., Goodall, R., Mortensen, A., Onck, P.R., De Hosson, J.T.M., 2008. Fracture behavior of low-density replicated aluminum alloy foams. Materials Science and Engineering A 496, 376–382.

Ashby, M.F., Evans, A., Fleck, N.A., Gibson, L.J., Hutchinson, J.W., Wadley, H.N.G., 2000. Metal Foams: A Design Guide. Butterworth, Heinemann.

Attard, M.M., Hunt, G.W., 2004. Hyperelastic constitutive modeling under finite strain. International Journal of Solids and Structures 41, 5327–5350.

Badiche, X., Forest, S., Guibert, T., Bienvenu, Y., Bartout, J., Ienny, P., Croset, M., Bernet, H., 2000. Mechanical properties and non-homogeneous deformation of open-cell nickel foams: Application of the mechanics of cellular solids and of porous materials. MSE A 289, 276–288.

Boonyongmaneerat, Y., Dunand, D.C., 2009. Effects of strut geometry and pore fraction on creep properties of cellular materials. Acta Materialia 57, 1373–1384.

Bouaziz, O., Bréchet, Y., Embury, J.D., 2008. Heterogeneous and architectured materials: a possible strategy for design of structural materials. Advanced Engineering Materials 10, 24–36.

Buffière, J.Y., Maire, E., Adrien, J., Masse, J.P., Boller, E., 2010. In situ experiments with X ray tomography: An attractive tool for experimental mechanics. Experimental Mechanics 50, 289–305.

Buffière, J.Y., Maire, E., Cloetens, P., Lormand, G., Fougères, R., 1999. Characterization of the internal damage in a MMCp using X-ray synchrotron phase contrast microtomography. Acta Materialia 47, 1613–1625.

Burteau, A., Bartout, J., Forest, S., Bienvenu, Y., Saberi, S., Naumann, D., 2008. Investigation of Representative Volume Element size for the mechanical properties of open-cell nickel foams. In: Lefebvre, L.P., Banhart, J., Dunand, D.C. (Eds.), 5th Biennial International Conference on Porous Metals and Metallic Foams (MetFoam 2007), Montreal, Canada, pp. 471–474.

Cailletaud, G., Forest, S., Jeulin, D., Feyel, F., Galliet, I., Mounoury, V., Quilici, S., 2003. Some elements of microstructural mechanics. Computational Materials Science 27, 351–374.

Cantournet, S., Desmorat, R., Besson, J., 2009. Mullins effect and cyclic stress softening of filled elastomers by internal sliding and friction thermodynamics model. International Journal of Solids and Structures 46, 2255–2264.

Caty, O., Maire, E., Youssef, S., Bouchet, R., 2008. Modeling the properties of closed-cell cellular materials from tomography images using finite shell elements. Acta Materialia 56, 5524–5534.

Combaz, E., Bacciarini, C., Charvet, R., Dufour, W., Mortensen, A., 2011. Multiaxial yield behaviour of Al replicted foam. Journal of the Mechanics and Physics of Solids 59, 1777–1793.

Dai, X., Sabuwala, T., Gioia, G., 2011. Lonsdaleite model of open-cell elastic foams: Theory and calibration. Journal of Elasticity 104, 143–161.

Dillard, T., Forest, S., Ienny, P., 2006. Micromorphic continuum modelling of the deformation and fracture behaviour of nickel foams. European Journal of Mechanics A/Solids 25, 526–549.

Dillard, T., N'Guyen, F., Maire, E., Salvo, L., Forest, S., Bienvenu, Y., Bartout, J.-D., Croset, M., Dendievel, R., Cloetens, P., 2005. 3D quantitative image analysis of open-cell nickel foams under tension and compression loading using X-ray microtomography. Philosophical Magazine 85, 2147–2175.

Diologent, F., Conde, Y., Goodally, R., Mortensen, A., 2009. Microstructure, strength and creep of aluminium-nickel open cell foam. Philosophical Magazine 89, 1121–1139.

Duchamp, M., Bartout, J., Forest, S., Bienvenu, Y., Walther, G., Saberi, S., Boehm, A., 2007. Mechanical properties of nickel-based superalloy foams for Diesel particle filter applications. In: Zhao, H., Fleck, N. (Eds.), IUTAM Symposium on Mechanical Properties of Cellular Materials, September 17–21, Paris, France, pp. 51–67.

Fazekas, A., Dendievel, R., Salvo, L., Bréchet, Y., 2002. Effect of microstructural topology upon the stiffness and strength of 2d cellular structures. International Journal of Mechanical Sciences 44, 2047–2066.

Fullwood, D.T., Niezgoda, S.R., Adams, B.L., Kalidindi, S.R., 2010. Microstructure sensitive design for performance optimization. Progress in Materials Science 55, 477–562.

Gagliardi, F., De Napoli, L., Felice, L., Umbrello, D., 2009. A comparison among FE models to simulate metallic foams forming – An experimental validation. Materials and Design 30, 1282–1287.

Gong, L., Kyriakides, S., Jang, W., 2005. Compressive response of open-cell foams. Part I: Morphology and elastic properties. International Journal of Solids and Structures 42, 1355–1379.

Goussery, V., Bienvenu, Y., Forest, S., Gourgues, A.-F., Colin, C., Bartout, J.-D., 2004. Grain size effect on the mechanical behavior of open-cell nickel foams. Advanced Engineering Materials 6, 432–439.

Jang, W., Kraynik, A., Kyriakides, S., 2008. On the microstructure of open-cell foams and its effect on elastic properties. International Journal of Solids and Structures 45, 1845–1875.

Kanit, T., Forest, S., Galliet, I., Mounoury, V., Jeulin, D., 2003. Determination of the size of the representative volume element for random composites: statistical and numerical approach. International Journal of Solids and Structures 40, 3647–3679.

Kaoua, S.A., Dahmoun, D., Belhadj, A.E., Azzaz, M., 2009. Finite element simulation of mechanical behaviour of nickel-based metallic foam structures. Journals of Alloys and Compounds 471, 147–152.

Laiarinandrasana, L., Piques, R., Robisson, A., 2003. Visco-hyperelastic model with internal state variable coupled with discontinuous damage concept under total Lagrangian formulation. International Journal of Plasticity 19, 977–1000.

Lantuéjoul, C., Maisonneuve, F., 1984. Geodesic methods in quantitative image analysis. Pattern Recognition 17 (2), 177–187.

Madi, K., Forest, S., Boussuge, M., Gallièque, S., Lataste, E., Buffière, J.Y., Bernard, D., Jeulin, D., 2007. Finite element simulations of the deformation of fused-cast refractories based on X-ray computed tomography. Computational Materials Science 39, 224–229.

Maire, E., Babout, L., Buffière, J.Y., Fougères, R., 2001. Recent results on 3D characterisation of microstructure and damage of metal matrix composites and a metallic foam using x-ray tomography. Material Science and Engineering A 319–321, 216–219.

Maire, E., Fazékas, A., Salvo, L., Dendievel, R., Souhail, Y., Cloetens, P., Letang, J., 2003. X-ray tomography applied to the characterization of cellular materials related finite element modeling problems. Composites Science and Technology 63, 2431–2443.

Mangipudi, K.R., Onck, P.R., 2011. Multiscale modelling of damage and failure in two-dimensional metallic foams. Journal of the Mechanics and Physics of Solids 59, 1437–1461.

Marcadon, V., Feyel, F., 2009. Modelling of the compression behaviour of metallic hollow-sphere structures: About the influence of their architecture and their constitutive material's equations. Computational Materials Science 47, 599–610.

Meyer, F., Beucher, S., 1990. Morphological segmentation. Journal of Visual Communication and Image Representation 1, 21–46.

Montminy, M., Tannenbaum, A., Macosko, C., 2004. The 3D structure of real polymer foams. Journal of Colloid and Interface Science 280, 202–211.

Ogden, R., 1984. Non-linear Elastic Deformations. Dover, New York.

Oppenheimer, S.M., Dunand, D.C., 2007. Finite element modeling of creep deformation in cellular metals. Acta Materialia 55, 3825–3834.

Ridha, M., Shim, V.P.W., 2008. Microstructure and tensile mechanical properties of anisotropic rigid polyurethane foam. Experimental Mechanics 48, 763–776.

Serra, J., 1988. Image Analysis and Mathematical Morphology, Vol. 2: Theoretical Advances. Academic Press.

Tekoglu, C., Onck, P.R., 2008. Size effects in two-dimensional voronoi foams: A comparison between generalized continua and discrete models. Journal of the Mechanics and Physics of Solids 56, 3541–3564.

Vicente, J., Topin, F., Daurelle, J.-V., 2006. Open celled material structural properties measurement: From morphology to transport properties. Materials Transactions 47, 2195–2202.

Walther, G., Klöden, B., Büttner, T., Weissgärber, T., Kieback, B., Böhm, A., Naumann, D., Saberi, S., Timberg, L., 2008. A new class of high temperature and corrosion resistant nickel-based open-cell foams. Advanced Engineering Materials 10, 803–811.

Warren, W., Neilsen, M., Kraynik, A., 1997. Torsional rigidity of a Plateau border. Mechanics Research Communications 24 (6), 667–672.

Youssef, S., Maire, E., Gaertner, R., 2005. Finite element modelling of the actual structure of cellular materials determined by X-ray tomography. Acta Materialia 53, 719–730.